TOPICAL STUDIES OF THE GEOLOGY OF THE THARSIS REGION OF MARS

Thesis

by

KARL RICHARD BLASIUS

In Partial Fulfillment of the

Degree of

Doctor of Philosophy

California Institute of Technology

Pasadena, California

1976

(Submitted August 15,1975)

PREFACE

This doctoral thesis consists of three independent papers on three separate research topics. The first two papers are being prepared for early publication while the last paper was published in July 1973 and is presented here in reprint form.

Drs. Eugene M. Shoemaker, Bruce C.Murray, and Robert P. Sharp provided substantial guidance to the work reported here. A large measure of gratitude is also extended to those who helped the author prepare high quality photographic materials for study and illustration. At the Image Processing Laboratory (Jet Propulsion Lab, Pasadena, Ca.) these include James Soha, Joel Seidman, Arnold Schwartz, Michael Wolf, Reuben Ruiz, Alan Gilespie, Fred Akers, and William Green. At Caltech the photographic talents of Jurrie J. van der Woude and Terrance Allen were indispensable.

Leanna Blasius deserves a special award for patience on the home front and for typing early drafts of this thesis from my primitive handwriting.

These studies were partially supported by NASA Grant NGR 05-002-302.

ABSTRACT

I.

Mariner IX images of the four great volcanic shields of the Tharsis region of Mars show many circular craters ranging in diameter from one hundred meters to twenty kilometers. Previous attempts to date the volcanoes from their apparent impact crater densities yielded conflicting results. The principal difficulty is sorting volcanic from impact craters for diameters $<$1km. Many of the observed craters are aligned in prominent linear and concentric patterns suggestive of volcanic origin. In this paper an attempt is made to date areas of shield surface, covered with high resolution images using only scattered small ($\leq$ 1 km) craters of probable impact origin. In some cases a fraction of the visible craters, those of apparent volcanic origin, is systematically excluded from the dating counts.

The common measure of age, deduced for all surfaces studied, is a calculated "crater age", F', defined as the number of craters equal to or larger than 1 km in diameter per $10^6 km^2$. The conclusions reached from comparing surface ages and their geological settings are:

1. Lava flow terrain surfaces with ages, F', from 180 to 490 are seen on the four great volcanoes. Summit surfaces of similar ages, F'=360 to 420, occur

on the rims of calderas of Arsia Mons, Pavonis Mons, and Olympus Mons. The summit of Ascraeus Mons is possibly younger; F' is calculated to be 180 for the single area which could be dated.

2. One considerably younger surface, $F' \lesssim 110$, is seen on the floor of Arsia Mons' summit caldera.
3. Nearly crater free lava flow terrain surfaces seen on Olympus Mons are estimated to be less than half the age of a summit surface. The summit caldera floor is similarly young.
4. The pattern of surface ages on the volcanoes suggests that their eruption patterns are similar to those of Hawaiian basaltic shields. The youngest surfaces seem concentrated on the mid-to-lower flanks and within the summit calderas.
5. The presently imaged sample of shield surfaces, though incomplete, clearly shows a broad range of ages on three volcanoes--Olympus, Arsia, and Pavonis Mons.

Estimated absolute ages of impact dated surfaces are obtained from two previously published estimates of the history of flux of impacting bodies on Mars. The estimated ranges of age for the observed crater populations are 0.5 to 1.2 billion years and 0.07 to 0.2 billion years. Areas which are almost certainly younger, less than 0.5 or

0.07 billion years, are also seen. The spans of surface age derived for the great shields are minimum estimates of their active lifetimes, apparently very long compared to those of terrestrial volcanoes.

II

Three types of large-scale mass movements - rockslides, slumps, and a type of mass flowage have been tentatively identified in photographs of the basal escarpment of the Martian volcano Olympus Mons. The morphology of slide deposits suggests lubrication of their movements by cushions of compressed gas. Gas trapped from the present rarefied atmosphere is probably insufficient, but a denser atmosphere in the past or the release of gases adsorbed on surface materials may provide adequate slide lubrication. Slumps occur widely along the north and southeast reaches of basal scarp and are mantled in the southeast by some of the youngest lava flows observed on Olympus Mons. The initiation of mass flowages, confined to two areas along the west reach of basal scarp, probably required a major change in the physical properties of surface materials. Chemical alteration of surface materials or the melting of ground ice, both possibly related to volcanism, might effect such a change.

Differences in escarpment morphology and mass movements suggest considerable recession of the west and north reaches of basal scarp and only slight recession, primarily by

slumping, of the southeast scarp. Low scarps on the plains near the foot of the southeast basal scarp and the apparent tilt of grooved terrain surfaces suggest the southeast reach of basal scarp formed by subsidence or downwarping along the margin of the volcano.

III

Many overlapping pictures, potential data for the construction of topographic maps, were obtained by the television cameras on Mariner 9. An analysis of the sources of error in photogrammetric determinations of relief from these pictures singles out photo resolution as the primary limiting factor. Topographic maps of several Martian surface features, derived by an original analytic scheme, are presented. The observed errors in relief determinations using this technique are in good agreement with the independent error analysis.

TABLE OF CONTENTS

LIST OF ILLUSTRATIONS

LIST OF TABLES

I. THE RECORD OF IMPACT CRATERING ON THE GREAT VOLCANIC SHIELDS OF THE THARSIS REGION OF MARS

Introduction

Among the most startling discoveries of the 1971-72 Mariner IX Mars orbiter mission was a group of volcanoes in and near the region with the classical name Tharsis (Fig. 1). The region in which the volcanoes occur, which is several thousand kilometers across, coincides approximately with a broad upland (Christensen, 1974 and Fig. 2) and a large positive free air gravity anomaly (Sjogren, et al., 1974). Both the topographic and the gravitational anomalies of the Tharsis region are by far the largest such features on Mars, encompassing approximately 30% of the surface area of the planet. Four of the volcanoes--Olympus, Arsia, Pavonis, and Ascraeus Mons (Figs. 3 and 4) have lateral dimensions in excess of 300 km. These volcanoes are widely spaced across the summit and flanks of the upland (Figs. 1 and 2). Their study might be expected to provide clues to the processes of internal evolution which have led to the development of the topographic high and mass accumulation on one side of the planet. In particular, knowledge of the relative ages of the four great volcanoes would be of fundamental interest.

The spatial density of impact craters has proven to be a valuable tool for determining relative ages of lunar surfaces (i.e., Shoemaker and Morris, 1970: Soderblom, 1970). Its application to Mars has been limited primarily by the

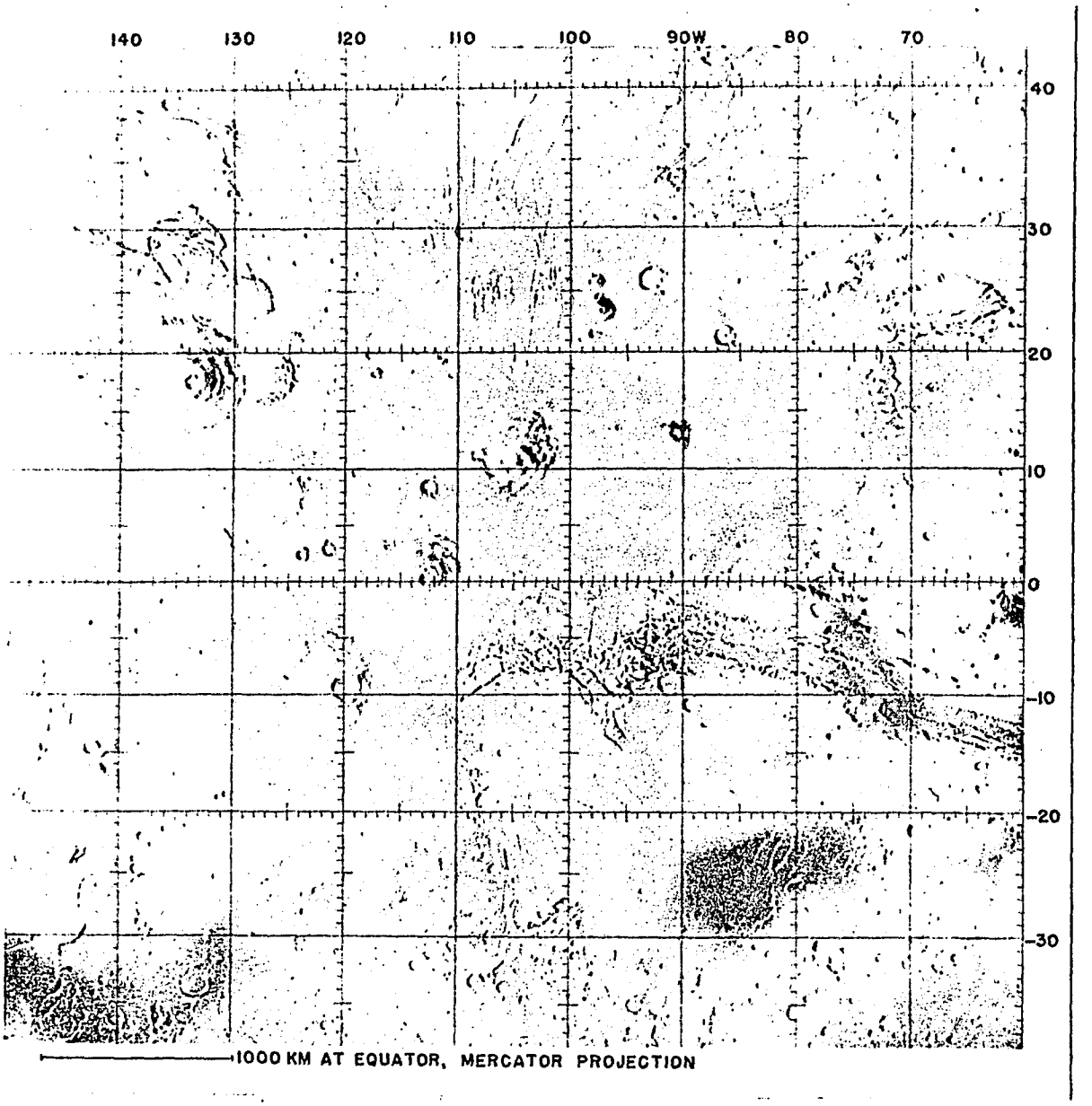

Figure 1. Airbrush map (Lowell Observatory, 1973) of the Tharsis region of Mars, which includes four great shields and several smaller volcanoes. Topographic features are drawn from Mariner 9 photos while regional differences in albedo are based on telescopic observations.

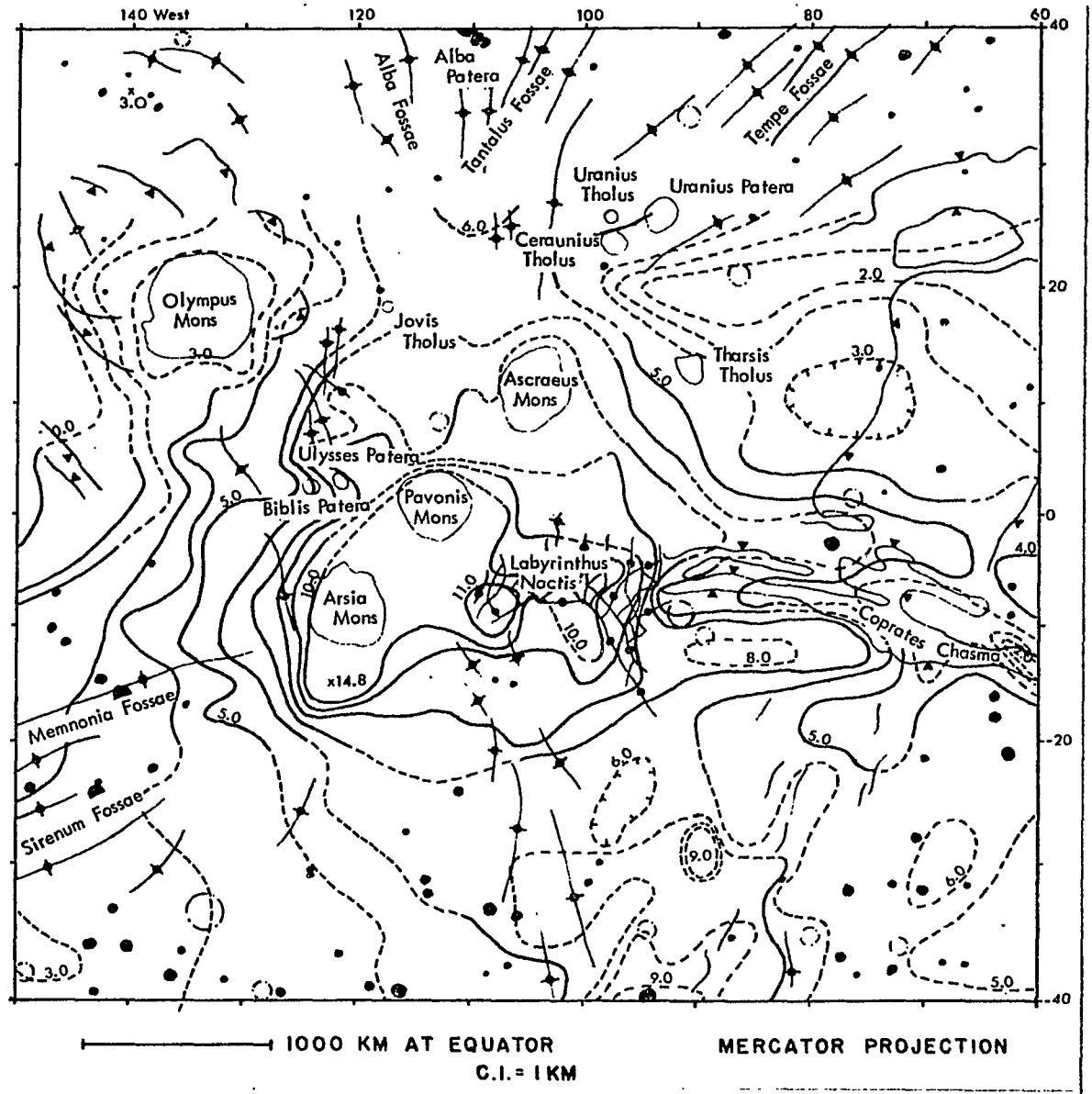

Figure 2. Topographic map and key to geographical names for the Martian upland centered in the Tharsis region. Data from Earth-based radar and the Mariner 9 S-band occultation, infrared spectrometer, and ultraviolet spectrometer experiments have been integrated, averaged in 2.5° squares, and hand contoured. Elevations are in km above the 6.1 mb areoid. Averaged data were provided by E.J. Christensen of the Jet propulsion Laboratory (personal communication, 1974). Figure 1 is an air brush rendering of Mariner 9 images of this region.

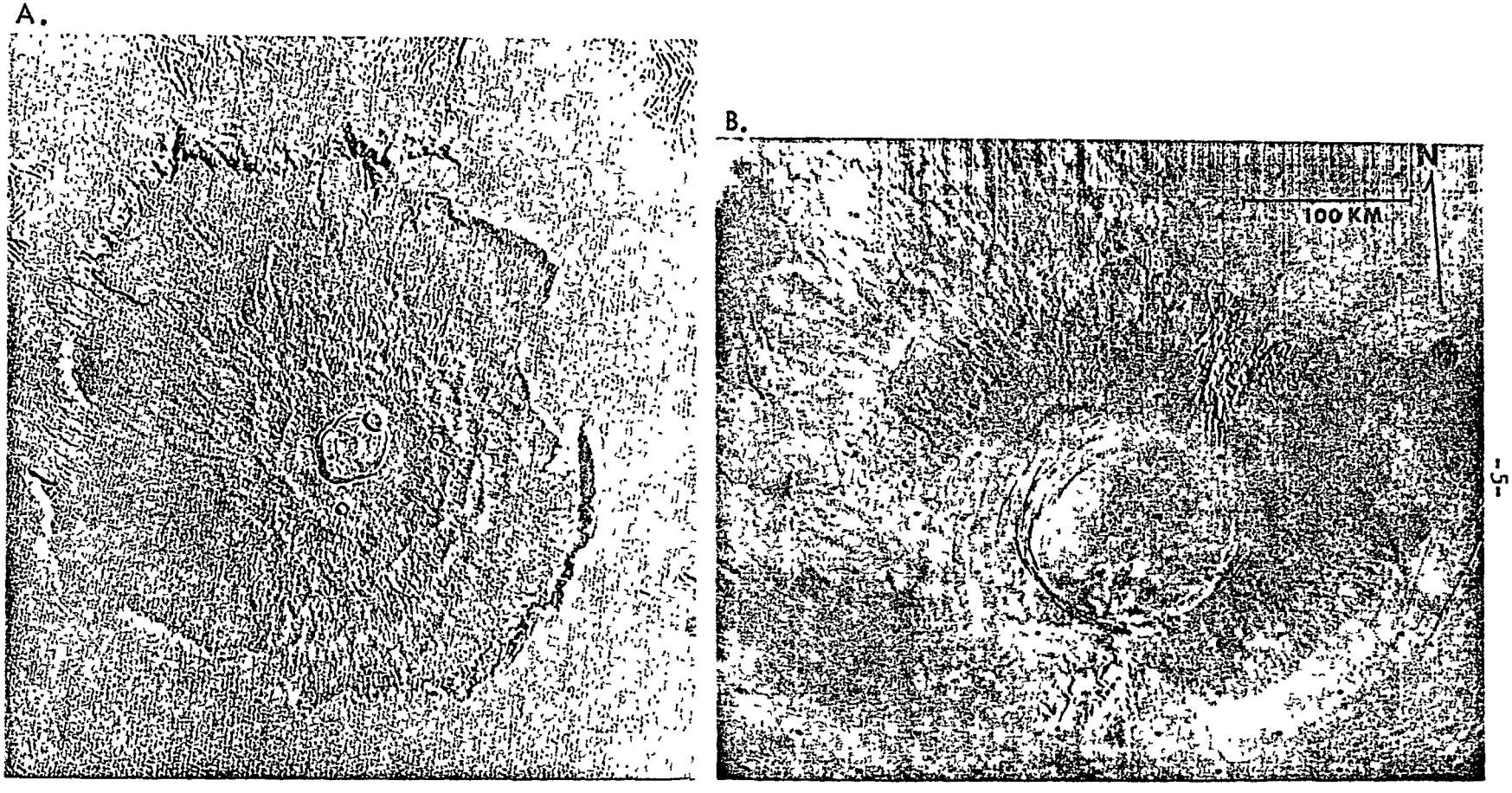

Figure 3. A) Mosaic of five enhanced low resolution images of Olympus Mons volcano. The images (DAS 6823428, 6823708, 6823778, 6895668, and 6895738) were mosaiced by computer according to a mercator projection at the Image Processing Lab, Jet Propulsion Laboratory, Pasadena, Ca.
B) Enhanced low resolution image (DAS 8441904) of Arsia Mons volcano.

A.

B.

Figure 4. A) Mosaic of two enhanced low resolution images (DAS 7111128, 7111198) of Pavonis Mons volcano.
B) Mosaic of six enhanced low resolution images (DAS 7111268, 7111338, 7111408, 7111618, 7183298, 7183368) of Ascraeus Mons volcano.

problem of assessing the poorly understood effects of erosional episodes. Jones (1974), Hartmann (1973), and Soderblom, et al., (1974) have, however, made planetwide interpretations of martian geology using cratering data. In the last two studies, the great volcanoes of the Tharsis region of Mars were found to be relatively young. Crater populations on the great volcanoes should thus have suffered little modification by the peculiar erosional and depositional regimes hypothesized for early martian history. The discussion here will assume that each observed crater population represents the total formed since the local surface was last renewed.

Atmospheric shielding of Mars' surface from impacting objects poses a potential problem for comparing crater densities on Mars and the Moon. This effect appears to be negligible, however, for the craters studied here, which are larger than about 100m in diameter. A recent investigation of the theory of meteorite -atmosphere interactions (Gault, unpublished manuscript) suggests that passage through the martian atmosphere will not significantly affect objects which produce craters larger than about 100m in diameter.

Observed variations in shield morphology generally support the assumption of no loss of small impact craters. Taking into consideration the lighting and viewing geometry of the images, lava flow features down to the limit of resolution appear sharp and uneroded. With the exception of parts of the western flanks of the great shields, the lava flow terrains of shield flanks and summits appear to be degraded primarily by the accumulation of aeolian sediment; landsliding possibly is important locally. The small features of lava flows would be mostly buried by aeolian blankets before craters of the size considered in this study had been filled. Assurance against loss of a significant part of the impact record can therefore be achieved by studying surfaces which exhibit the characteristic small features of lava flows.

Soderblom, et al., (1974) found that the modification of small craters by aeolian deposition was primarily controlled by global atmospheric circulation and, perhaps secondarily, by elevation. The great volcanoes all lie within an equatorial zone characterized by a minimum of blanketing by aeolian deposits and the similar high elevations of their flank surfaces should tend to equalize and minimize all types of aeolian modification of surface features. Populations of craters larger than 100m on the four great volcanoes probably can be compared and treated as a complete record of impact

on the exposed surfaces.

Previous Investigations

McCauley, et al., (1972) made the first attempt to date a martian volcano surface by study of the crater population. They derived an age of 4×10^7 years for Olympus Mons from counts of craters in a diameter range of 300m to 9km, under the assumption that the relatively recent cratering rate on Mars has been about 10 times that on the Moon.

Hartmann (1973) attempted to date a variety of martian surfaces, including volcano flanks, by scaling the flux of impacting objects on Mars with respect to the flux in the vicinity of the Earth according to specific assumptions concerning past abundances and orbits of the objects. He concluded that the recent flux on Mars was higher than that near Earth by a factor of 3 to 30. Combining this result with a reduced velocity of asteroidal objects relative to Mars, he estimated the effective cratering rate on Mars to be, within a factor of 3, 6.2 times the lunar rate. Terrestrial cratering data was then used to argue that impact fluxes have been nearly constant over the past three billion years. On this basis, Hartmann attempted to date absolutely some younger martian surfaces from their impact records.

Those surfaces of interest in this study are:

		Age (Hartmann, 1973)
1.	"Sparsely Cratered Volcanic Regions"--an average for the lightly cratered surfaces of the northern hemisphere of Mars, including most of the upland around Tharsis	3×10^8 yr
2.	Olympus Mons	1.3×10^8 yr
3.	Arsia Mons	2.0×10^8 yr
4.	Pavonis Mons	8.0×10^7 yr
5.	Ascraeus Mons	1.0×10^8 yr

A major problem in dating the volcanic shields is the presence of large numbers of small craters of volcanic origin. The resolution of Mariner IX images is adequate to classify only a small fraction of the visible craters as to volcanic or impact origin on the basis of single crater morphology. In dating Arsia Mons and Ascraeus Mons, Hartmann attempted to distinguish impact from volcanic craters over the entire diameter range 300m to 30km using only rim and interior morphology. In dating Pavonis Mons this method was abandoned, because:

"... the craters counted were, on most of the pictures,

> not readily distinguishable into impact and non-impact craters, but it was believed, on the basis of fault patterns, that some of the smaller craters may associate with chains and clusters of endogenic craters."

The date Hartmann derived was thus based on less abundant larger craters (> 2km in diameter). On the other hand, the age derived for Olympus Mons was based entirely on the total count of smaller craters (diameter <2km), justified on the basis that the form of the crater population closely resembled that of lunar impact crater populations at small diameters.

I believe that each of the criteria Hartmann has introduced to identify impact craters has some validity, though given the resolution of Mariner IX images, criteria based on details of a single crater morphology are useful for classifying only a small fraction of observed craters. Hartmann apparently has applied his criteria unsystematically. For example, he mentions structural alignments as a clue to the presence of volcanic craters only in connection with Pavonis Mons (Fig. 4A), but low resolution images show much larger numbers of aligned craters on Arsia and Ascraeus Mons (Figs. 3B, 4B).

On the basis of similar frequency distributions of crater spatial density on the surfaces of Mars and the Moon, Soderblom, et al., (1974) have concluded that the impact

histories of Mars and the Moon have been similar. In order to date geologic units widely distributed over Mars, particularly in regions with different conditions of aeolian erosion and deposition, they were forced to study craters in the 4 to 10 km diameter range. In applying their method to the surfaces of the volcanoes, Soderblom et al., were also confronted with the problem of recognition of impact craters, but they make no mention of attempting to exclude volcanic craters from their counts. Some approximate ages obtained by Soderblom et al., (1974) are:

		Age (Soderblom et al., 1974)
1.	Plains of the Tharsis upland	$0.2 - 0.8 \times 10^8$ yr
2.	Olympus Mons	$0.7 - 1.3 \times 10^8$ yr
3.	Arsia Mons	$5.9 - 8.0 \times 10^8$ yr
4.	Pavonis Mons	$1.4 - 2.4 \times 10^8$ yr
5.	Ascraeus Mons	$1.4 - 2.4 \times 10^8$ yr

The two sets of dates for the volcanoes are unsatisfactory when compared. If both studies used the same Mariner IX data and chose impact craters in a similar fashion, one would expect the relative ages of the volcanoes in each set of dates to be similar. Hartmann concludes that Olympus Mons is intermediate in age between the putatively older Arsia Mons, and the younger Ascraeus and Pavonis Mons. Soderblom, et al., however,

found Olympus Mons to be the youngest of the great shields. They also found Arsia Mons to be much older, relative to the other three great volcanoes, than did Hartmann. Clearly a reevaluation of the crater data is needed.

Identification of Populations of Small Impact Craters

In this report an attempt is made to overcome the problems encountered by previous investigators by applying explicit criteria for the separation of small craters according to their origin and by ignoring large craters, which are seen only in low resolution images and commonly are aligned. Moderate numbers of scattered small craters are observed in many high resolution images of surfaces on the great volcanoes. Unlike the larger craters seen in low resolution images, only a minor fraction of small craters seem to be structurally controlled. It seems promising, therefore, to attempt to segregate small impact craters from small volcanic craters. When probable volcanic craters have been identified, the statistical characteristics of the population of remaining craters may be compared with the characteristics of craters of presumed impact origin on the Moon. The criteria used here for identification of individual volcanic craters are:

1. Crater form is distinctly elongate;

2. The crater is part of a chain of three or more craters;
3. The crater falls along the trend of one or more linear or sinuous troughs.

These criteria are most useful when the population of non-aligned round craters is relatively large compared to the population of aligned or elongate craters; a few small, isolated, and circular volcanic craters must be expected to occur, and such craters cannot be distinguished from those of impact origin. To test the validity of these criteria, the populations of small craters in two areas of apparently nonvolcanic martian terrains were examined. The areas studied are two samples of heavily cratered upland of the martian southern hemisphere; image DAS 8261339 covers an area located 23° S., 337° W., and image 12499225 covers an area located 45°S., 161°W. Carr, et al., (1973) interpreted surface materials in these areas as most probably impact breccias modified primarily by aeolian processes. It was found that the criteria for identification of volcanic craters would apply to less than 3% of the small craters seen in these two areas. Crater counts from individual images were relatively large, 41 to 60. The numbers of craters excluded, as probably volcanic, from counts in each area on the volcanoes are listed in Table 1.

To further evaluate the impact origin of craters remaining after exclusion of volcanic craters identified by the above criteria, the following standards were applied:

1. All populations of remaining craters should have similar statistical form (Figs. 5 and 6). Populations of small impact craters have a characteristic slope, when plotted in standard form, of about -3 on lunar maria surfaces. Plots of crater data by Hartmann (1973) and Soderblom et al., (1974), for large areas of apparently nonvolcanic martian terrains, parallel lunar data.
2. The patterns of relative surface ages determined on each shield should be consistent with any morphological indicators of age. For example, the floors of volcanic vent craters are likely to be resurfaced more often than surfaces on a volcano's flank.

The first test of impact origin for a selected crater population is the slope of the distribution. It has been found that distributions of craters a few hundred meters to a few kilometers across on the lunar maria follow a power function (Shoemaker and Morris, 1970):

$$F(c, \lambda) = \chi\, c^{\lambda}$$

where F is the cumulative number of craters of diameter $\geq c$ per $10^6 km^2$. χ is variable from site to site, reflecting surface age, and λ is close to -3 everywhere. We should expect martian craters formed by impact to show a similar functional form. In Table 1 is listed the approximate slope

TABLE I. DATA ON SMALL CRATERS ON SURFACES OF GREAT VOLCANOES OF MARS

Volcano	Image DAS Time	Approximate Area		c_L, Smallest Diameter not Limited by Image Resolution	Total Craters	Probable Volcanic Craters	Cumulative Impact Crater Count at $c=c_L$	Apparent Slope of Distribution	F', Estimated Cumulative Impact Crater Density at c = 1 Km
Arsia Mons	4258460	665 Km^2	caldera floor	210 meters	22	0	18	-2.5	$250 \pm 50\ 10^{-6}\ Km^{-2}$
"	"	185	caldera rim	"	11	0	9	-2.3	420 ± 150
"	4330280	970	caldera floor	150	37	4	25	-4	90 ± 20
"	8369909	1000	caldera floor	300	10	0	9	-2.9	240 ± 80
"	"	1000	caldera rim	"	19	10	15	-1.3	------
"	7038713	1000	shield margin	190	12	0	10	-1.2	-----
Pavonis Mons	5779973	1150	caldera rim	244	24	0	22	-2.4	280 ± 40
"	4402170	1150	depression floor	250	20	2	17	-3.4	230 ± 60
"	7111163	1550	depression floor	320	12	0	11	-1.7	———
"	"	650	depression rim	"	10	0	10	-2.9	490 ± 300
"	5563953	2300	caldera rim	470	21	8	8	-3.0	360 ± 120
Ascraeus Mons	5636473	2600	caldera rim	264	34	1	26	-2.8	180 ± 40
Olympus Mons	9557319	4100	shield flanks	440	17	5	12	-3.6	250 ± 90
"	9557459	2800	shield flanks	400	10	0	10	-3.1	230 ± 70
"	5492413	2230	shield flanks	300	30	8	19	-4.7	-----
"	8297879	1900	near summit	440	15	0	9	-2.4	400 ± 140

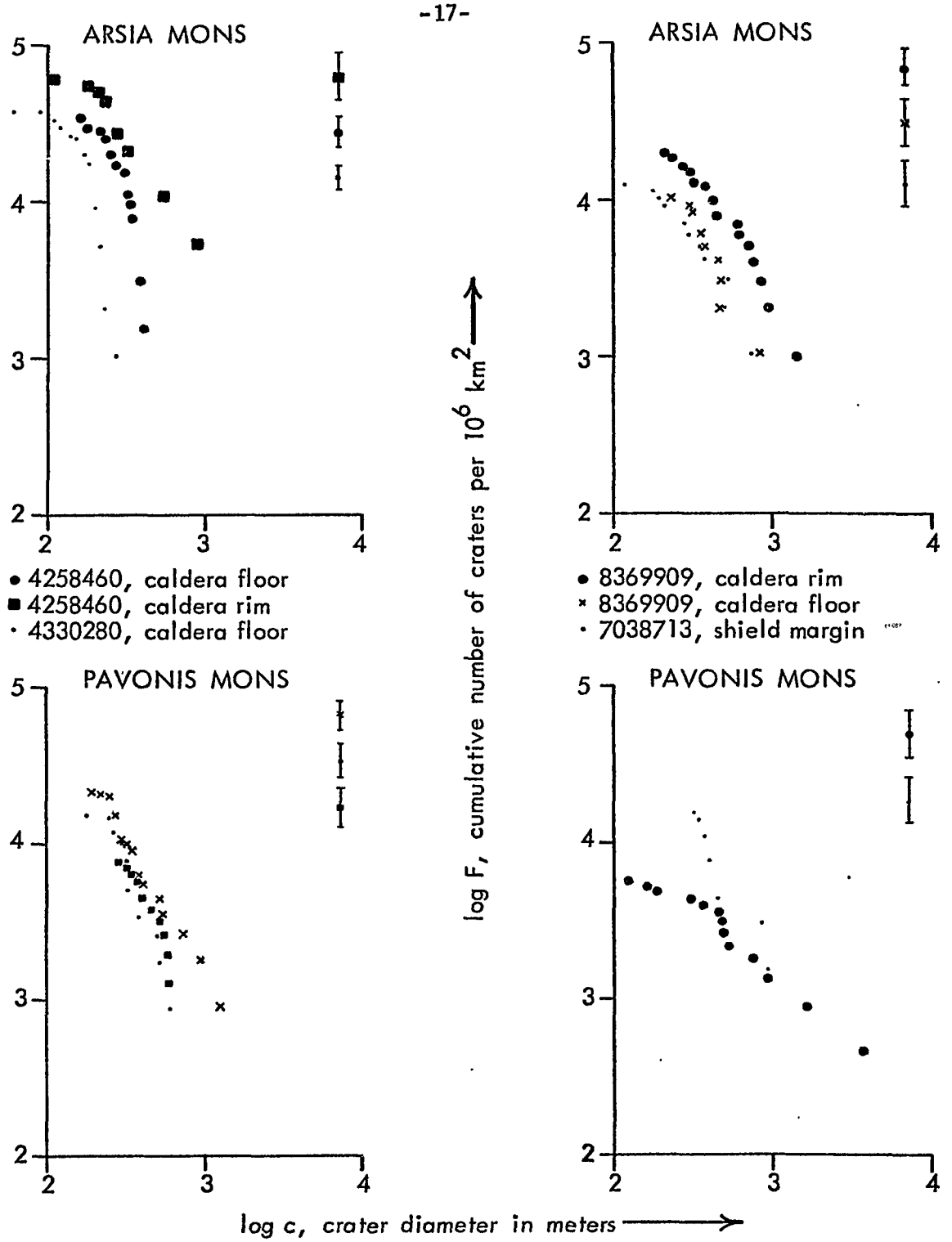

Figure 5. Plots of cumulative crater density versus crater diameter for several areas seen at high resolution on Arsia Mons and Pavonis Mons. Minimum error bars shown apply to the cumulative impact crater density at $c=c_L$ (see text).

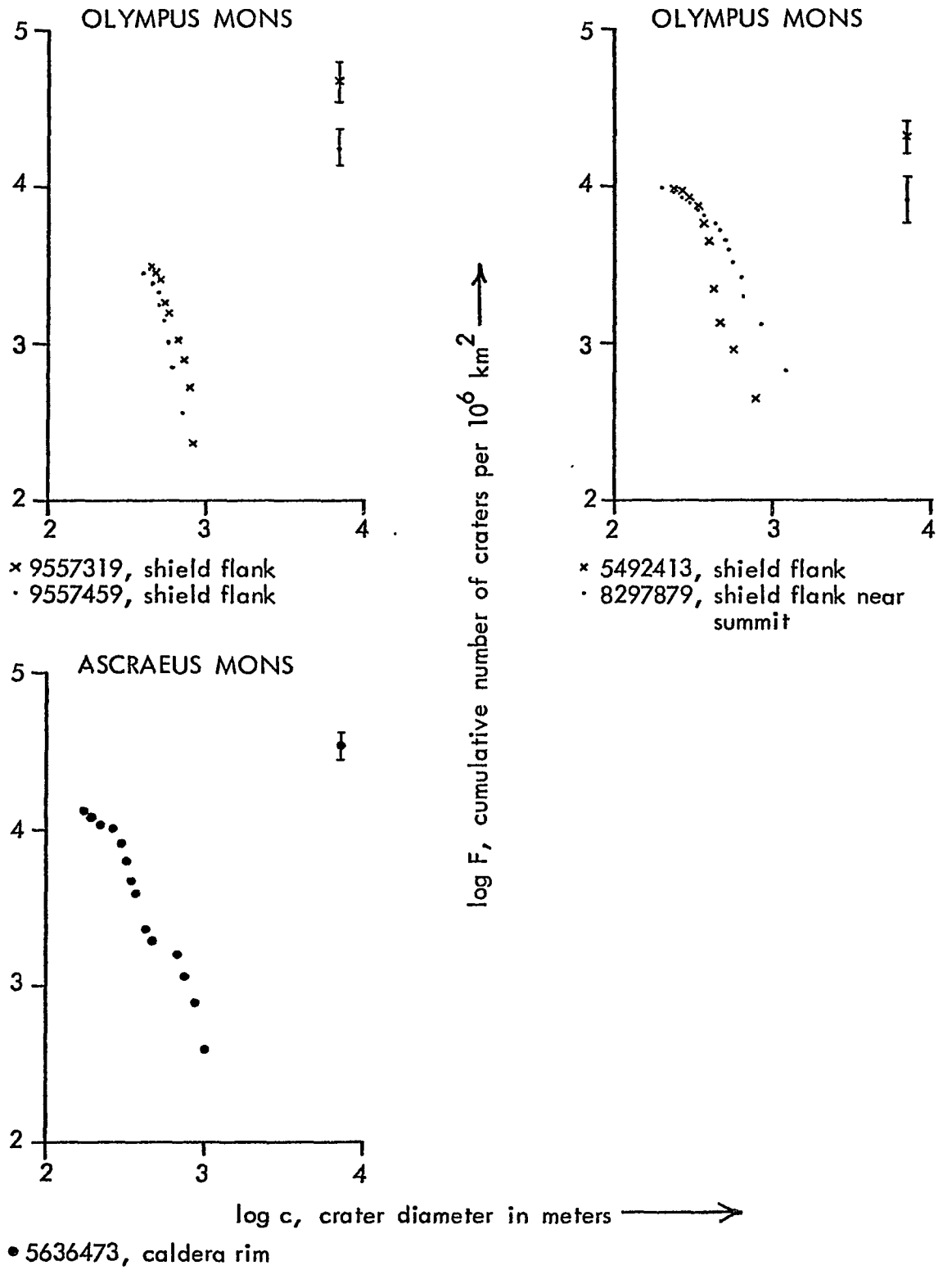

Figure 6. Plots of cumulative crater density versus crater diameter for several areas seen at high resolution on Olympus Mons and Ascraeus Mons. Minimum error bars shown apply to the cumulative impact crater density at $c=c_L$ (see text).

of the statistically most significant part of each crater distribution, near the small diameter end. It is clear that they cluster near -3. The mean slope is -2.8. There are, however, some distributions whose slopes are far from the mean. Possible reasons for deviations will be noted as each case arises in the discussion. Soderblom et al., (1974) found a similar slope for unmodified martian impact crater populations with diameters $\lesssim$ 1 km.

In order to compare all the plotted crater distributions, the statistically most significant part of each distribution is extrapolated to a standard crated diameter. The most significant part of a distribution contains the largest crater count unaffected by image resolution. Most crater distributions decline in slope at their small diameter end where a significant number of craters go unrecognized as the crater diameter approaches image resolution. The diameter at which the distribution begins to turn over seems to be consistently equivalent to 3 or 4 picture elements (pixels). The most significant crater counts and the corresponding diameters are listed in Table 1. To determine relative ages by comparing populations at a common diameter it is necessary to pick an arbitrary diameter, c and a value of the distribution slope, λ , to extrapolate to it. One km and -3 are adopted as values for c and λ , respectively. Calculated values of $F' \equiv F(1\ km,-3)$ should then reflect the relative ages of surfaces. If the flux of impacting objects has been roughly constant, the age of a surface will be

approximately proportional to F'.

Probable errors on the values of F' (Table 1) were calculated from the assumption that impact cratering follows a Poisson distribution. This means that the probability of a cratering event in a given area is proportional to that area. The standard deviation in a crater count, n, is then just $\sqrt{n}$, and the error on F' is $\pm \frac{\sqrt{n}}{n} F'$. Another source of error in F', more difficult to evaluate, is the uncertainty in the assumed distribution slope of -3. Use of a slightly different value will yield different absolute values of F' but will leave unchanged their relative magnitudes. In this study I am primarily interested in obtaining a measure of relative crater densities, so the exact precision of the assumed distribution slope is unimportant.

Plots of crater diameter versus cumulative density for all significant crater populations which passed the three volcanic crater elimination criteria are shown in Figures 5 and 6. Several presumably young surfaces, lacking crater populations of probable impact origin, are not indicated in these figures, but they will be mentioned in the discussion of each volcano.

Impact Craters on Arsia Mons

Six crater populations from Arsia Mons are plotted in Figure 5. Five are located at the shield summit. Two of

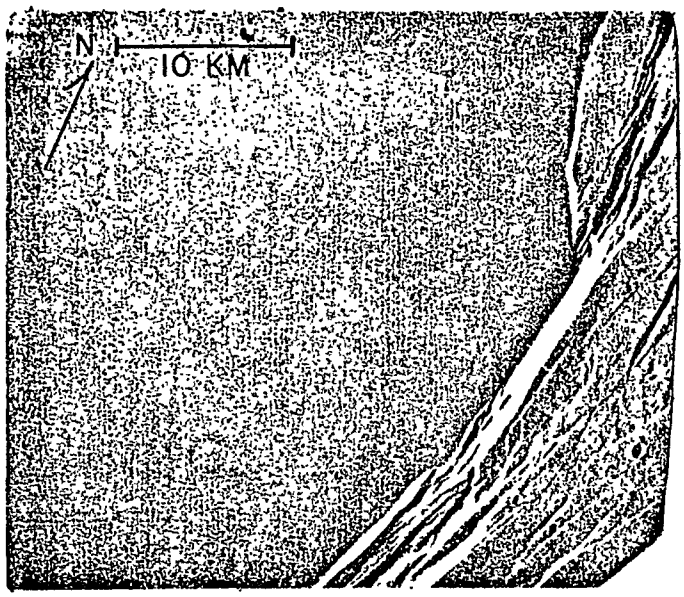

Figure 7. Southeast floor and fractured rim of Arsia Mons' summit caldera (DAS 4258460).

these are seen in image DAS 4258460 (Fig. 7) of the eastern caldera floor and rim. Table 1 indicates that the error bars on the impact ages for the two areas just touch, suggesting that the caldera floor is younger than the rim. The slopes derived from the distributions are very similar and relatively close to the mean for all distributions. Since no craters were excluded from the counts, it appears that volcanic craters are relatively unimportant here.

Two other caldera floor samples were counted. Image DAS 4330280 shows the apparently flat central caldera floor. Several small troughs and a crater chain were excluded from the count. These features are aligned parallel to rilles and crater chains on the northeast flank of the volcano (Fig. 3B). The steep distribution slope, -4, perhaps warns of additional volcanic craters. The high crater count, in part attributable to the best surface resolution achieved on any of the volcanoes, translates into small error bars on the F' (Table 1). This number should probably be viewed more as an upper limit to the impact flux age since the slope of the distribution is peculiar.

The northeast caldera floor and fractured rim were studied from image DAS 8369909. The most significant points in the floor crater distribution give a slope of -2.9, but the distribution of rim craters has a slope of only about -1.3. A contamination of the crater count by relatively large

volcanic collapse pits on the rim is a possible explanation for the peculiar slope. There is a high spatial density of troughs and crater chains of all sizes on the adjacent northeast flank of Arsia Mons (Fig. 3B).

The final small crater population observed on Arsia Mons is far down on the western flank in image DAS 7038713. The terrain appears to consist of lava flows which have experienced some aeolian erosion. Features observed which are characteristic of wind sculpting (McCauley, 1973) include fluted scarps and small parallel ridges. Many of the small craters are elongate in the direction of orientation of the scarp fluting and ridges. In view of the evidence of erosion, a deficiency of small craters might be expected. The crater distribution (Fig. 4) suggests such a deficiency by its shallow slope of only -1.2 (Table 1).

All the crater ages, F', derived for Arsia Mons are shown in Figure 8. We can now assess the possible geological significance of the differences in ages. The general pattern of frequency of surface renewal on Hawaiian basaltic shields seems to favor mid-to-lower flank eruptions, probably because of higher pressures lower in the magma column (MacDonald, 1972). Eruptions which flood portions of caldera floors are also very common. The lowest frequencies of surface renewal seem to be at the summit outside the caldera and at the farthest margins of a shield, which are reached only by exceptionally long flows. The limited

pattern of ages

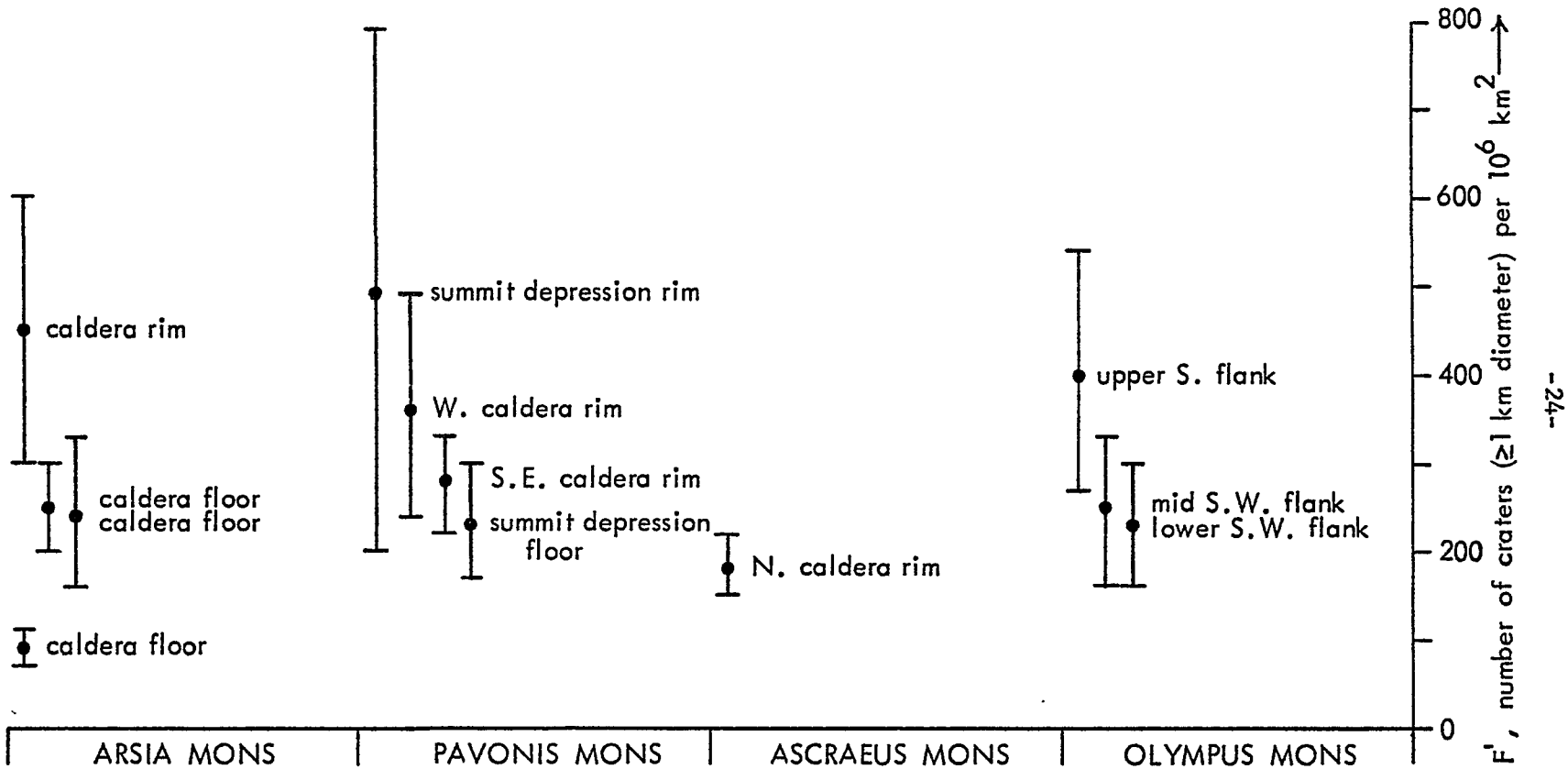

Figure 8 . Surfaces on the four great volcanoes are compared by their estimated crater densities for diameters ≥1 km. Surfaces of similar age are found on all four volcanoes. Crater counts are plotted in Figures 5 and 6 . Other data on individual areas are listed in Table 1 .

found on Arsia Mons seems to fit this pattern. The caldera rim appears to be older than two samples of caldera floor, and one sample is decidedly younger than the other three dated surfaces. It is reasonable, too, that the youngest area of caldera floor is its center. Gentle down-warping over an internal magma reservoir, such as those hypothesized to exist within Hawaiian shields (Eaton and Murata, 1960), might make the central caldera floor the area most easily reflooded by lava during later eruptions.

Several areas of Arsia Mons should be noted for their lack of definable impact crater populations. Only a single subdued 600 m crater is seen (in DAS 7038783) on the rugged terrain of the volcano's northwest flank (Fig. 3B). Perhaps this area is a region of relatively deeply eroded terrain. The uppermost valleys appear to be cut into the surface which forms the caldera rim.

The northeast foot of Arsia Mons and adjacent plains (DAS 8441939) also lack recognizable impact craters. The volcano flank is marked by abundant troughs and crater chains while three of the six small craters seen on the adjacent plains are aligned suggesting they are volcanic in origin.

Impact Craters on Pavonis Mons

Most high resolution images of Pavonis Mons are of the summit. This is a very complex area, and all summit terrains

have small craters. The caldera floor and southeast rim are shown in DAS 5779973 (Fig. 9). Only two small craters are visible on the floor, so a minimum impact flux age cannot be derived. Neither is it possible to place a confident upper limit on the flux age. The upper face of the caldera wall is fluted suggesting widespread landsliding. Dust raised by landsliding within the caldera of Fernandina (Galapagos Islands) formed deposits up to several meters thick (Simkin and Howard, 1970); impact craters on the floor of Pavonis Mons' caldera may have been buried by analogous deposits.

The caldera rim has many more craters. Their distribution is plotted in Figure 5. The distribution slope of -2.4 (Table 1) supports the impact hypothesis.

The generally flat floor of a broad summit depression to the north and east of the caldera, is shown in two images, DAS 4402170 and DAS 7111163. The craters seen in the first image may be primarily of impact origin, as the distribution has a slope of -3.4. The population in DAS 7111163 is probably contaminated with volcanic craters, however, as the crater distribution slope is -1.7. The crater age derived from DAS 4402170 should probably be considered an upper limit because of the presence of probable volcanic craters nearby on another part of the floor of the summit depression.

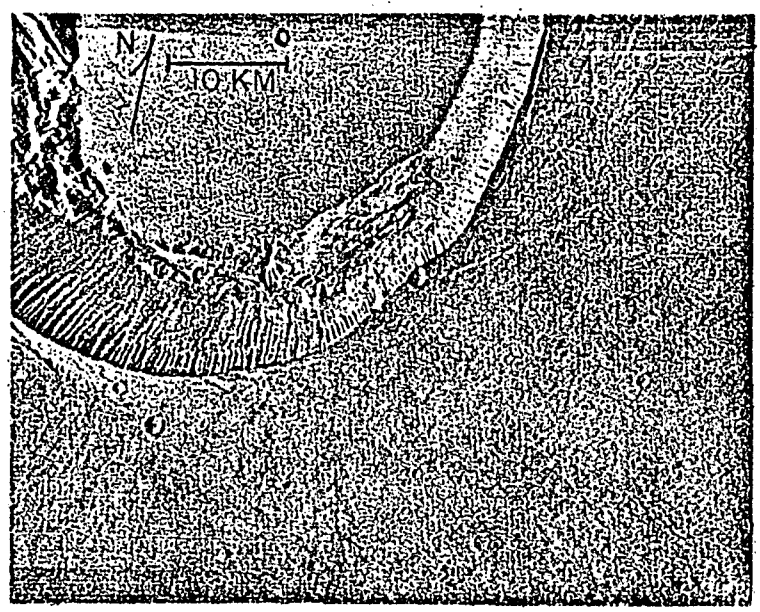

Figure 9. Floor and southeast rim of Pavonis Mons' summit caldera (DAS 5779973).

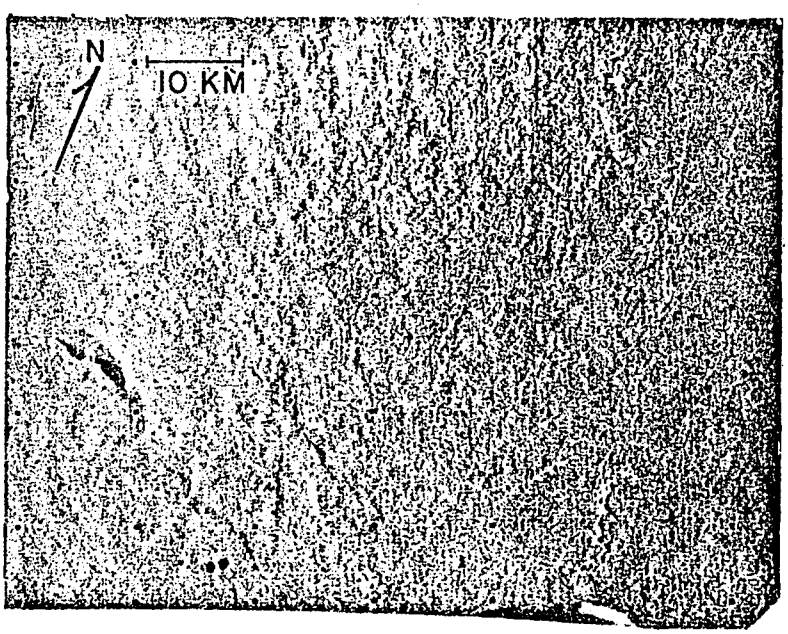

Figure 10. North rim of summit caldera and upper flank of Ascraeus Mons (DAS 5636468).

Other surfaces for which crater ages may be obtained are the western caldera rim (DAS 5563953) and the northeastern rim of the summit depression (DAS 7111163). In the first case a relatively large number of volcanic craters were identified. Crater counts are small, so error bars on the crater ages are large (Table 1, Fig. 8).

The ages of surfaces on Pavonis Mons' summit are mostly very similar. The only dated surface that may be significantly younger than the others is the floor of the summit depression. This younger age is consistent with the pattern of ages observed on Arsia Mons, if the broad summit depression is structurally equivalent to a caldera.

Impact Craters on Ascraeus Mons

Only one image of a datable surface is available for Ascraeus Mons. Image DAS 5636468 (Fig. 10) shows the north rim of the caldera. Illumination is very oblique so crater visibility is ideal. A total of 26 craters of probable impact origin were counted (Fig. 6). The slope of -2.8 supports this identification (Table 1), and the crater age is similar to ages derived for surfaces on the other volcanoes (Fig. 8). The summit surface on Ascraeus Mons appears to be slightly younger than those seen outside calderas on the other volcanoes.

Undatable surfaces on Ascraeus Mons include the southern caldera rim (DAS 8729914). A large percentage of the small craters form crater chains, so no population of probable

impact craters can be separated. Another undatable surface is on the northern flank of Ascraeus Mons (DAS 5636468). Volcanic craters of all sizes, aligned concentrically about the volcano's summit, are the principal features in this area.

Impact Craters on Olympus Mons

The varied high resolution coverage of Olympus Mons provides the only samples of impact crater populations on the mid-level flanks of a shield. DAS 9557314 (Fig. 11) shows a population of small craters in flow terrane on the volcano's southwest flank. A chain of five craters, aligned approximately downslope, was excluded from the crater count. The distribution has a slope of -3.6 (Table 1). A similar number of craters was counted lower on the southwest flank where lava flows are in contact with a much smoother terrain (DAS 9557459). The lava flow terrain has a crater age very similar to that derived for the surface higher on the southwest flank (Fig. 11).

The image of Olympus Mons with the best surface resolution (DAS 5492413; Fig. 12) appeared to be a promising subject for impact crater dating. However, the many small craters, excluding two crater chains, have a decidedly nonimpact distribution with a steep slope of -4.7 (Table 1). This lava flow terrain has a fresh undegraded appearance; the steep slope of the size-frequency distribution may be

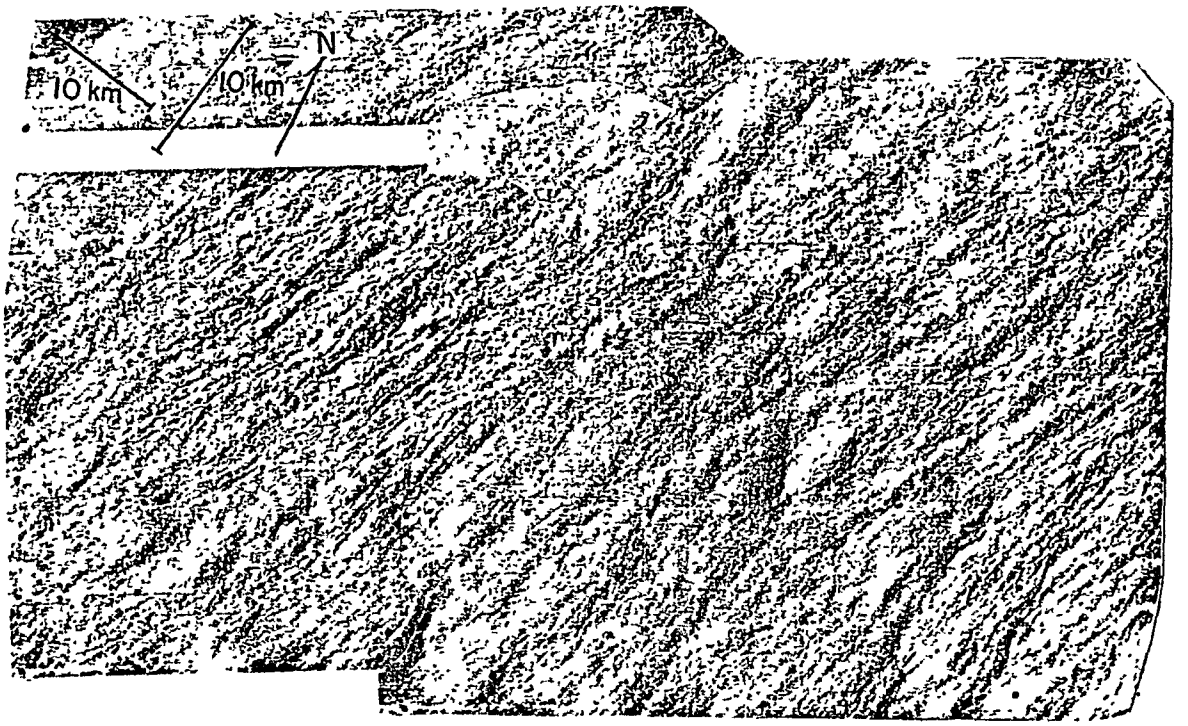

Figure 11. Photomosaic of an area on Olympus Mons' southwest flank (DAS 9557314 and 9557384).

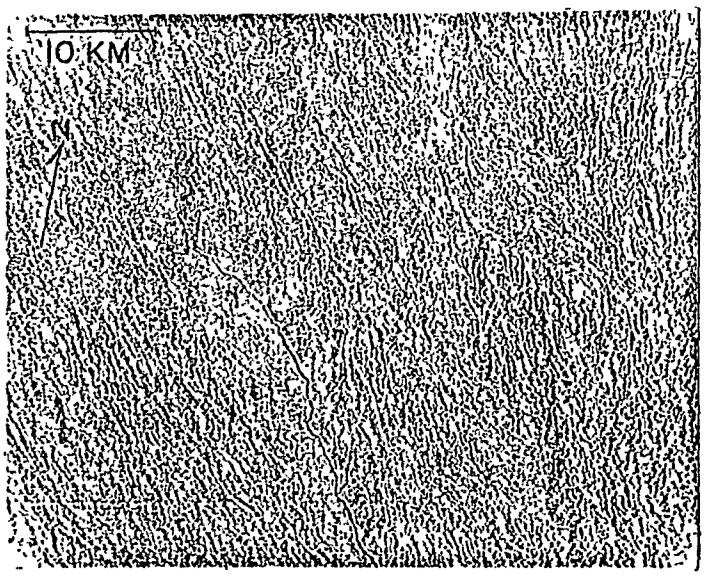

Figure 12. Part of Olympus Mons' northwest flank (DAS 5492413).

due to an excess of volcanic pits at the small diameter end of the distribution.

Another population of probable impact craters is seen in DAS 8297874, which shows lava flow terrain just south of the summit of Olympus Mons. The crater age (Table 1) suggests that this surface is older than the lower flank surfaces, a relationship which is consistent with the eruption patterns on Hawaiian volcanic shields.

Data from surfaces with insignificant numbers of impact craters are also consistent with Hawaiian shield eruption patterns. High resolution images of apparently fresh flows on the lower southeast and north flanks of the shield (DAS 6895698 and 9701239) show only four craters larger than about 500 m across in an area of 7250 km^2. A maximum F' of 104 (1σ) to 139 (2σ) is implied. The floor of the summit caldera also appears to be young compared to flank surfaces examined. No craters larger than 500 m across are seen in an area of about 3000 km^2. This implies a maximum F' of about 83 (1σ) to 166 (2σ).

Conclusions

The basic conclusions reached from this study of crater ages of areas on the great Tharsis volcanoes are:

1. Lava flow terrain with ages, F', from 180 to 490 are seen on the four great volcanoes. Summit surfaces of similar ages, F'=360 to 420, occur outside the

calderas of Arsia Mons, Pavonis Mons, and Olympus Mons. The summit of Ascraeus Mons is possibly younger: F' is calculated to be 180 for the single area which could be dated.

2. One considerably younger crater population, $F' \lesssim 110$, is seen on the floor of Arsia Mons' summit caldera.

3. Nearly crater free lava flow surfaces seen on Olympus Mons are estimated to be less than half the age of an area near the caldera rim. The summit caldera floor is similarly young.

4. The pattern of surface ages on the volcanoes suggests that their eruption patterns are similar to those of Hawaiian basaltic shield volcanoes. The most frequently renewed surfaces are on the mid-to-lower flanks and within summit calderas.

5. The presently imaged sample of great volcano surfaces on Mars, though incomplete, clearly shows a broad range of ages on three volcanoes--Olympus, Arsia and Pavonis Mons.

The present surfaces of these volcanoes, small samples of which are dated here, probably represent only a thin deposit from the last local eruptions. The range of impact crater ages derived for a volcano is a minimum estimate of its active lifetime. The oldest dates are derived for surfaces located at the volcano summits, so the great shields probably had attained essentially their present sizes by

those early dates.

Possible absolute ages of impact crater dated surfaces may be obtained from the martian flux history derived by Soderblom et al., (1974). This derived flux history is similar to that of the Moon. F' of 120 corresponds to an age of about 300 million years, and the flux of impacting objects is assumed approximately constant for the last 3 billion years. Using these scaling rules, most dated surfaces on the great shields range in age from 0.5 to 1.2 billion years. The youngest surfaces are estimated to date from the period approximately 0.5 billion years ago to the present. The oldest dated surfaces suggest that the great volcanoes had attained essentially their present sizes over 1 billion years ago. The broad range of surface ages seen on individual volcanoes indicates that these features are very long-lived compared to terrestrial volcanoes, with lifetimes greater than 1 to 1.5 billion years. Corresponding absolute ages based on Hartmann's (1973) martian impact flux history can be approximated by dividing all the above absolute ages by a factor of 6.2.

REFERENCES CITED

Carr, M.H., Masursky, H., and Saunders, R.S., 1973, A Generalized Geologic Map of Mars: J. Geophysical Res., v.78, p. 4031 - 4036.

Christensen, E.J., 1974a, private communication, Mars topographic map.

Christensen, E.J., 1974b, Martian Topography Derived from Occultation, Radar, Spectral, and Optical Measurements: submitted to J. Geophysical Res.

Eaton, J.P. and Murata, K.J. 1960, How Volcanoes Grow: Science, v.132, p. 925 - 938.

Gault, D., 1974, unpublished manuscript on the meteorite shielding effects of Mars' atmosphere.

Hartmann, W.K., 1973, Martian Cratering IV: Mariner 9 Initial Analysis of Cratering Chronology: J. Geophysical Res., v.78, p. 4096 - 4116.

Jones, K.L., 1974, Evidence of an Episode of Crater Obliteration Intermediate in Martian History: J. Geophysical Res., v.79, p. 3917 - 3931.

Macdonald, G.A., 1972, Volcanoes: Englewood Cliffs, New Jersey, Prentice-Hall, 510 p.

McCauley, J.F., 1973, Mariner 9 Evidence for Wind Erosion in the Equatorial and Mid-Latitude Regions of Mars: J. Geophysical Res., v.78, p. 4123 - 4138.

McCauley, J.F., Carr, M.H., Cutts, J.A., Hartmann, W.K., Sharp, R.P., and Wilhelms, D.E., 1972, Preliminary Mariner 9 Report on the Geology of Mars: Icarus, v.17, p. 289 - 327.

Shoemaker, E.M. and Morris, E.C., 1970, Physical Characteristics of the Lunar Regolith Determined from Surveyor Television Observations: Radio Science, v.5, p. 129 - 155.

Simkin, T. and Howard, K.A., 1970, Caldera Collapse in the Galapagos Islands, 1968: Science, V. 169, p. 429 - 437.

Sjogren, W.L., Lorell, J., Wong, L., and Downs, W., 1974, Mars Gravity Field Based on a Short-Arc Technique: submitted to J. Geophysical Res.

Soderblom, L.A., 1970, The Distribution and Ages of Regional Lithologies in the Lunar Maria: California Institute of Technology Ph.D. Thesis, 139p.

References - (continued)

Soderblom, L.A., West, R.A., Herman, B.M., Kreidler, T.J., and Condit, C.D., 1974, Martian Planetwide Crater Distributions: Implications for Geologic History and Surface Processes: Icarus, v.22, p. 239 - 263.

II. MASS MOVEMENT PHENOMENA ALONG THE BASAL SCARP OF OLYMPUS MONS, MARS

INTRODUCTION

The great volcanic shield Olympus Mons sits far down on the northwest flank of a broad equatorial upland (Figs. 1 and 2). Other probable volcanic features, including extensive plains, interpreted as lava, and central volcanoes, occupy much of the upland (Carr, 1973). Among the central volcanoes Olympus Mons is exceptional for its basal breadth of 500 km, relief of about 23 km and for an escarpment which defines much of its perimeter (Fig. 3, 4, and 5). The basal escarpment of Olympus Mons is particularly prominent along the west, north, and southeast margins of the volcano (Fig. 3). In these reaches features suggestive of mass movement are seen. Elsewhere the basal scarp is more subdued and mass movements are not recognized.

Character of the West and North Reaches of Basal Scarp

The face of the basal scarp to the west and north is deeply embayed. Spurs and blocky promontories extend as much as 40 km from the escarpment brink, but the brink is more smoothly arcuate in plan than the base, with indentations mostly less than 10 km deep. The west segment of the escarpment is 4 to 8 km high as determined from low-resolution stereo images (Fig. 5).

In low resolution ($\sim$ 2 km) images the face of the scarp appears smooth or locally benched, but high resolution images (Figs. 7 and 8) show a more complex character. The upper scarp face and the upper flanks of spurs are scored by

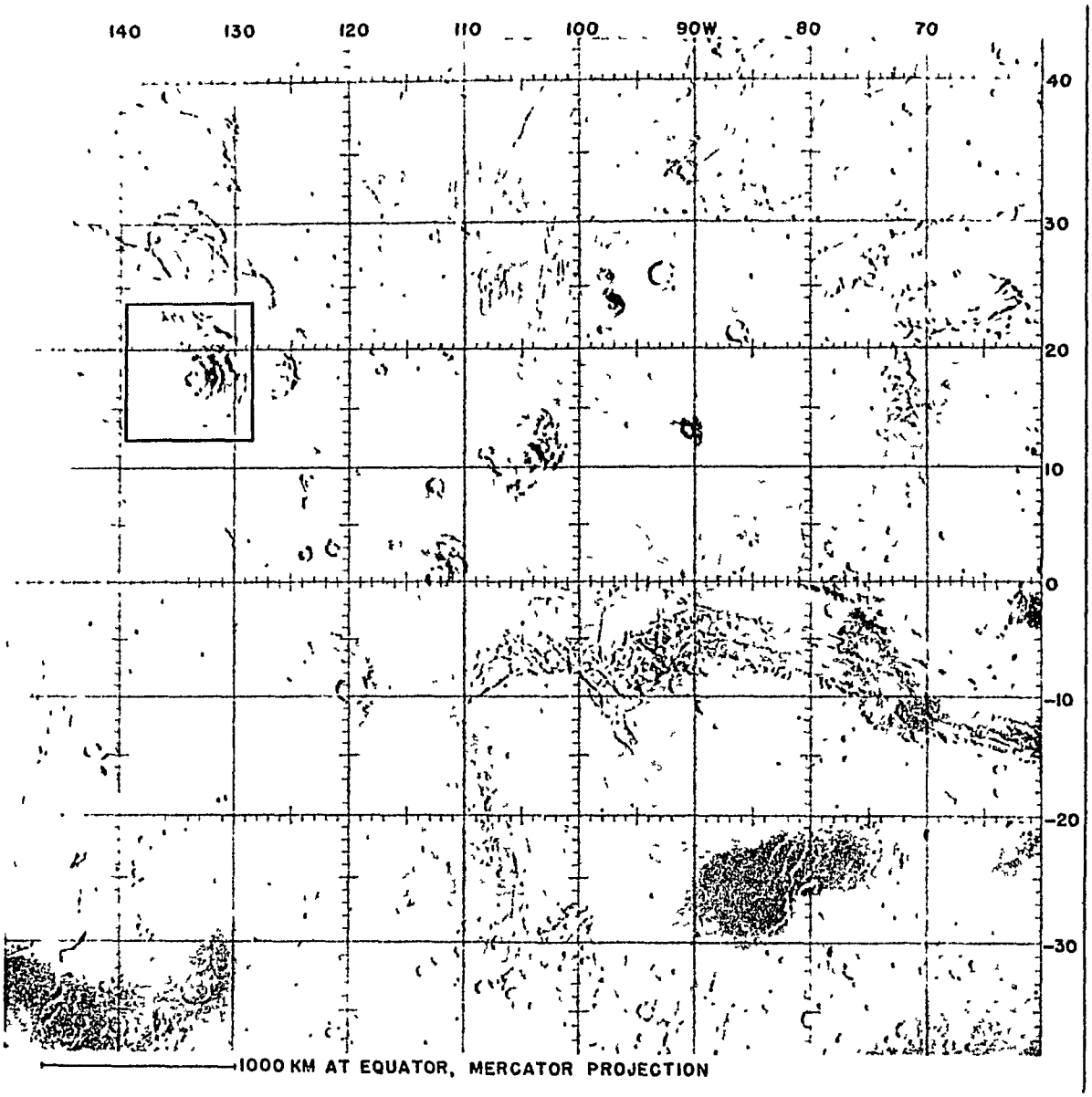

Figure 1. Airbrush map (Lowell Observatory, 1973) of the Tharsis region of Mars, which includes Olympus Mons (outlined) and several other large and small volcanoes. Topographic features are drawn from Mariner 9 photos while regional differences in albedo are based on telescopic observations from Earth.

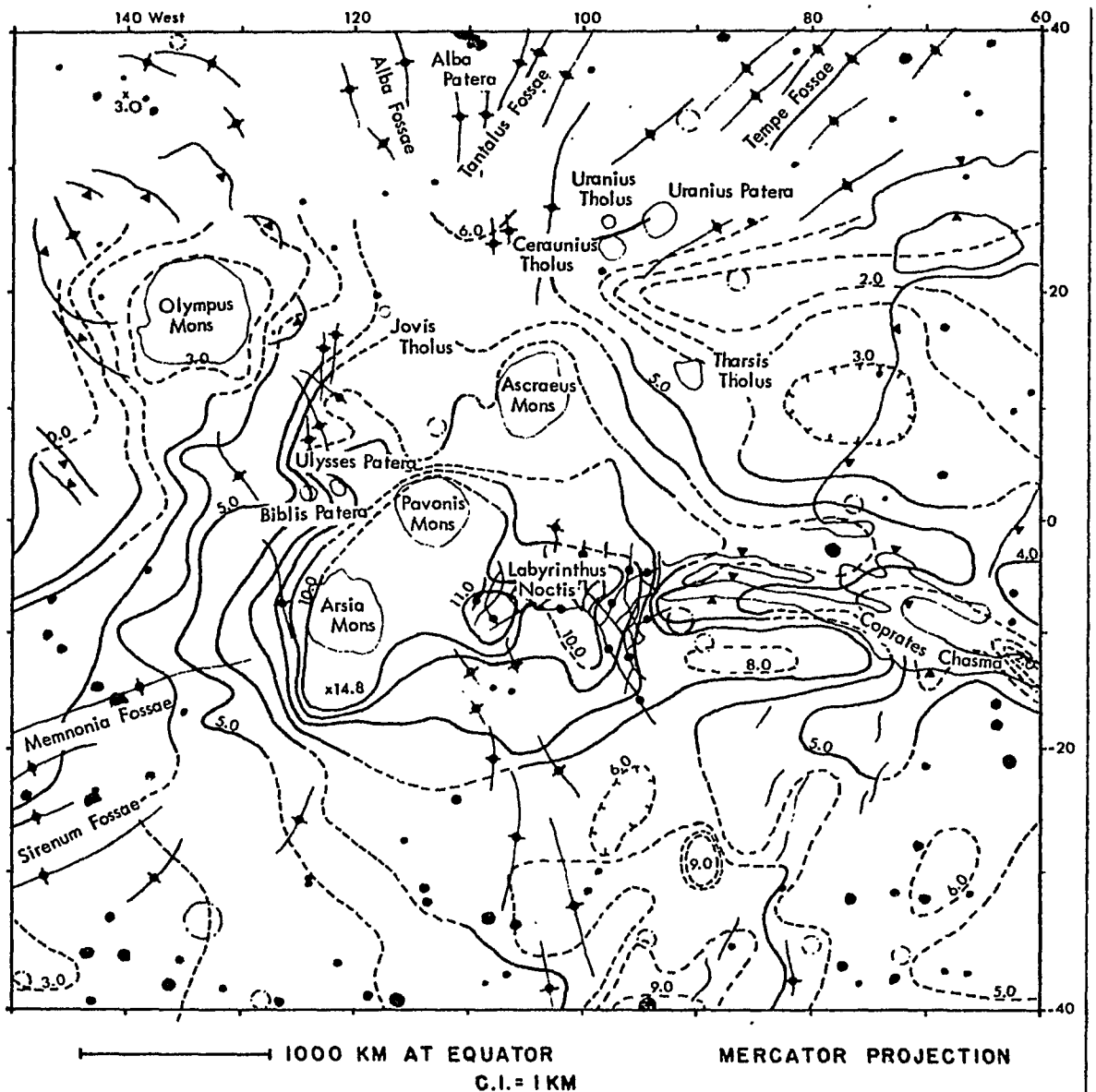

Figure 2. Topographic map and key to geographical names of the Martian upland centered in the Tharsis region. Data from earth-based radar and Mariner 9 experiments have been combined, averaged in 2.5° squares, and hand contoured. Averaged data were provided by E.J. Christensen of the Jet Propulsion Laboratory, Pasadena, Ca. (private communication, 1974).

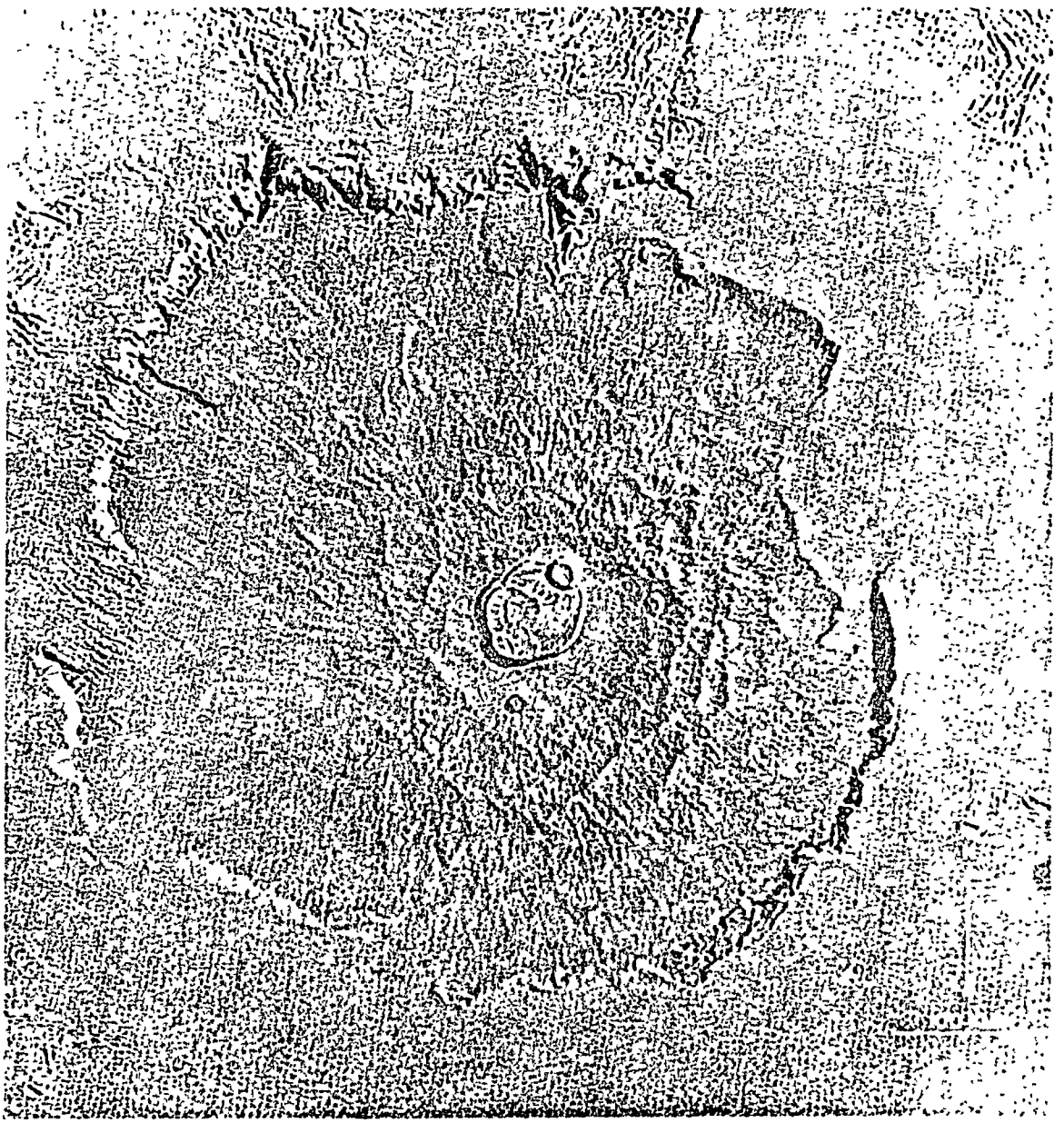

Figure 3. Photomosaic of Olympus Mons volcano. Five low resolution Mariner 9 photos (DAS 6823428, 6823708, 6823778, 6895668, 6895738) were enhanced and mosaicked by computer to mercator projection.

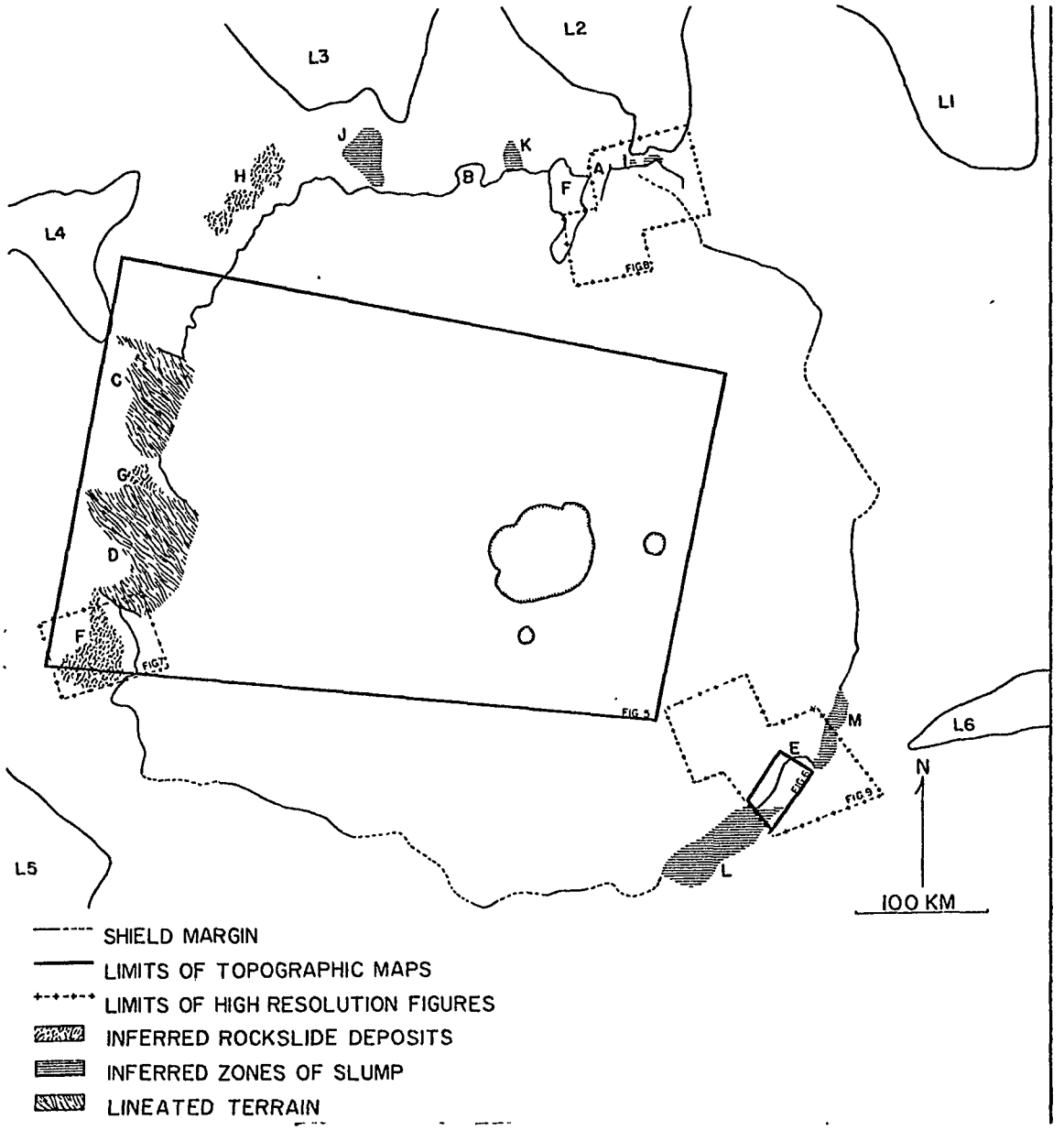

Figure 4. Key to coverage of high resolution photographs (Figs. 7 to 9), topographic maps made from stereo photos (Figs. 5 and 6), and locations of inferred mass movement terrains at the base of Olympus Mons. Letters identify terrain features discussed in text.

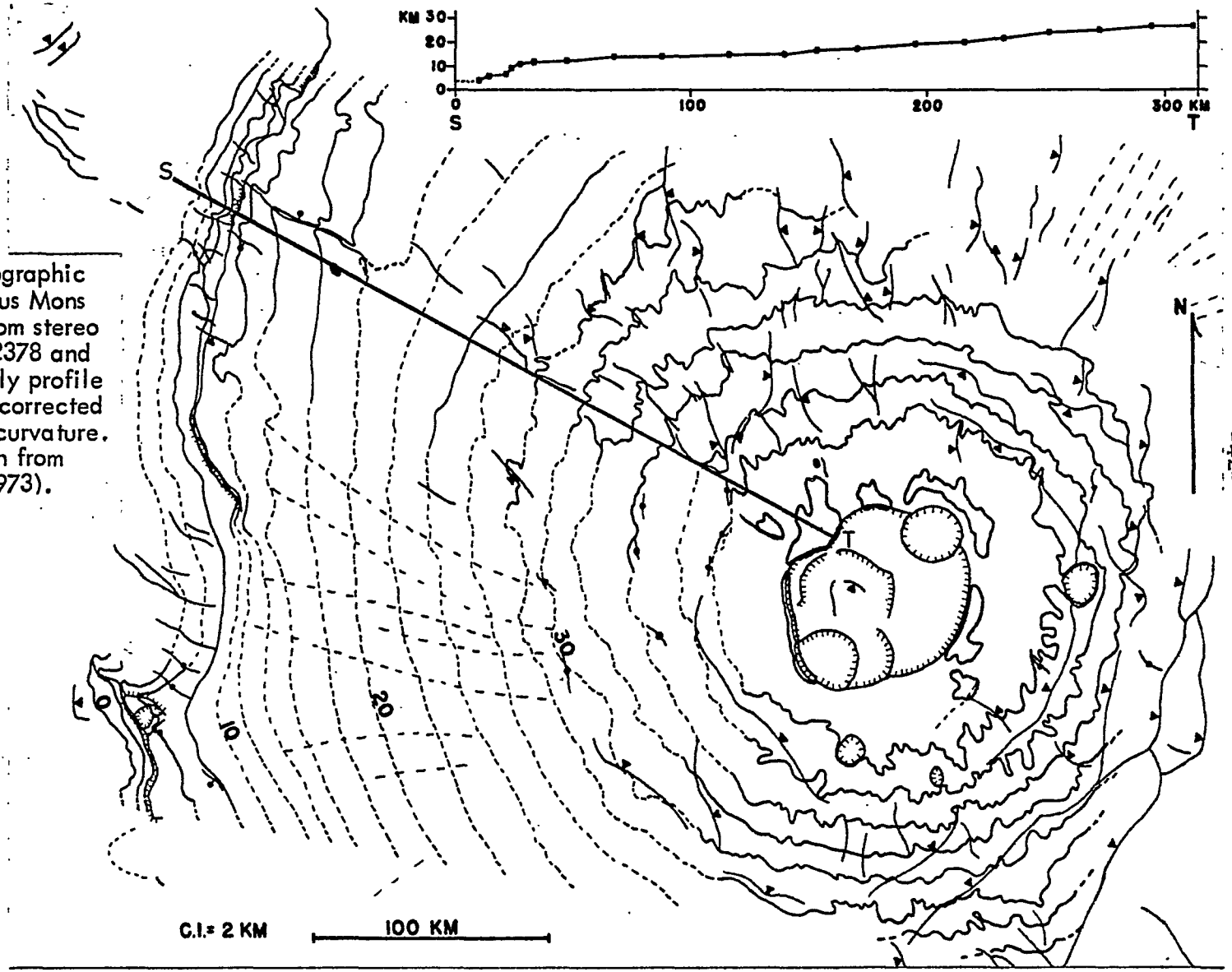

Figure 5. Topographic map of Olympus Mons constructed from stereo pair DAS 5492378 and 6823918. Only profile topography is corrected for planetary curvature. Data are taken from Wu, et al. (1973).

parallel downslope flutes spaced 300m (the limit of resolution) to 800m apart. Individual flutes vary little in width but differ one from the other in size by a factor of 2. In most places the lower half to two-thirds of the scarp face appears smooth down to the foot. Locally, under low oblique illumination, these lower reaches appear to be made up of adjacent conical segments 1 to 2 km across at the base (A in Fig. 7).

The west and north basal scarp is interrupted by subdued reaches for distances of 15 to 100 km in several places. In two of these, A and B in Figure 4, the relatively smooth flank of Olympus Mons extends down to the basal plain. In high-resolution photos these transition slopes display fine linear and curvilinear downslope markings. In two other reaches (C and D in Fig. 4) of the west basal scarp, slightly steepened slopes are roughened by ridges and troughs extending directly downslope.

Character of the Southeast Reach of Basal Scarp

The southeast reach of the basal scarp displays a different character. In low-resolution photos the scarp face consists of three to five benches separated by steep slopes. These subsidiary scarps are mostly 10 to 15 km but locally up to 50 km long. Spurs are lacking and the escarpment is indented at large scale in only one location (E in Fig. 4) where the scarp trends east-west for 30 km. Stereo images show part of the southeast reach of basal scarp

to be 4 to 6 km high and slope 20° (Fig. 6).

High-resolution images (Fig.9) show details of the central section of southeast basal scarp. Both northeast and southwest of the 30 km E-W reach, the scarp is benched, but the E-W reach is an enormous simple scarp about 6 km high (Fig. 6). Its upper face is fluted and the slope below is generally smooth. Scarps bounding some benches have a similar character, but most are more subdued and show only faint downslope lineations. Favorable illumination reveals that the smooth lower faces of scarps, at least locally, consist of adjacent conical segments (R in Fig. 9).

Relation of Basal Scarp to the Flanks of Olympus Mons

The flanks of Olympus Mons become distinctly smoother within 50 to 100 km of the basal escarpment (Fig. 3), and have decreasing slope outward (Fig. 5). Along profile ST (Fig. 5) the slope change is from about 5° to about 2°, and it occurs approximately where the flank becomes smoother. Shading in unfiltered images approaching the southeast reach of the basal scarp is consistent with these changes in slope and roughness there also.

Relation of Basal Scarp to Plains around Olympus Mons

Relatively smooth, sparsely cratered plains partly encircle the base of Olympus Mons (Carr et al., 1973). The scarp-plains contact involves a sharp break in slope as shown in high resolution images (Figs. 7, 8, and 9). Plains are replaced by areas of rough terrain locally along

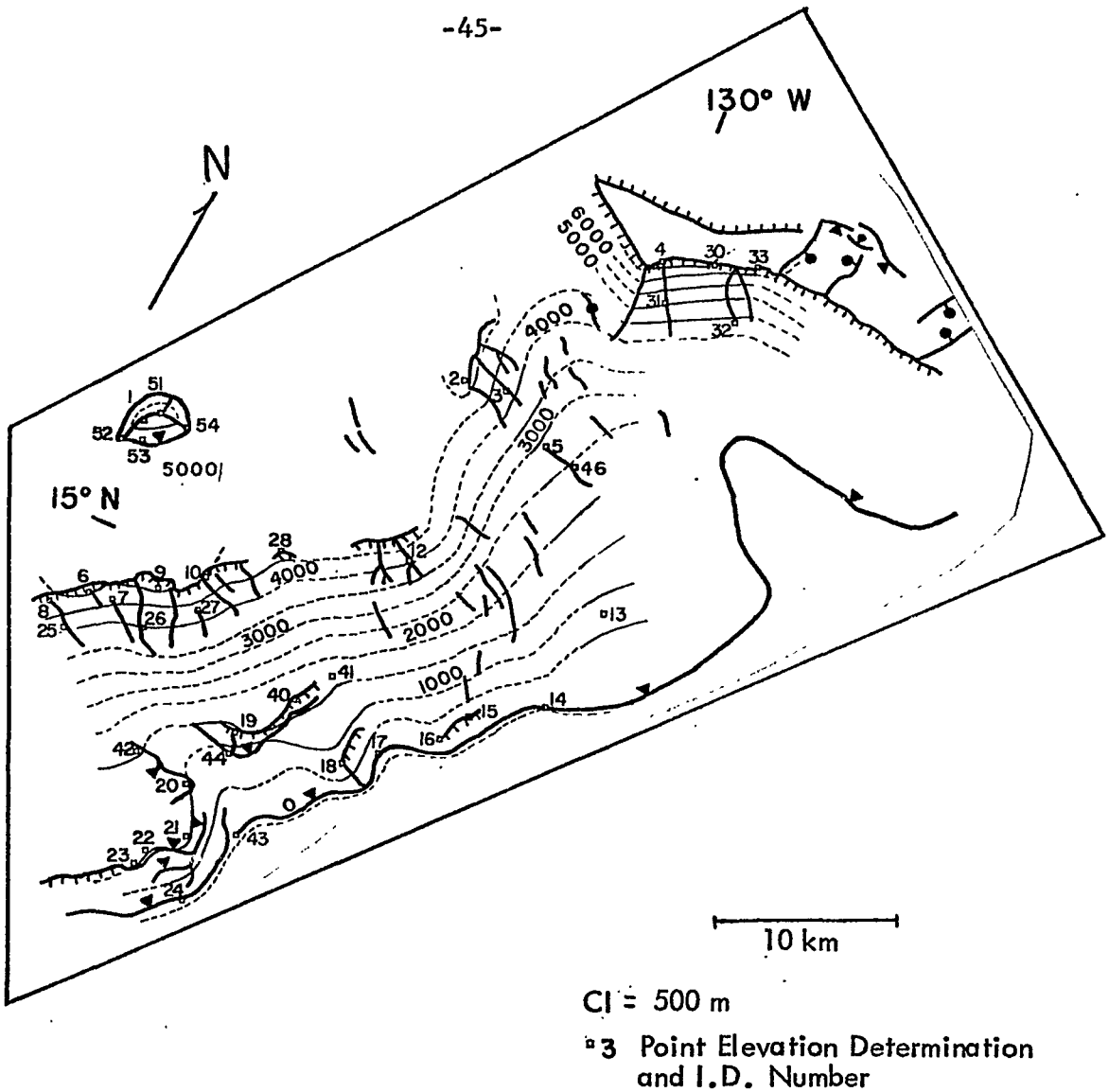

Figure 6. Topographic map of a part of the southeast basal scarp of Olympus Mons. Contours are interpolated between point elevation determinations listed in Table 1. Terrain symbols are defined in Figure 2. Data were derived from Mariner 9 stereo photos DAS 9844599 and 9845299.

TABLE I: Relative elevations of points on topographic map of the southeast reach of basal scarp (Fig. 6). All heights are ± 100 m.

Point	Model Height (m)	Point	Model Height (m)	Point	Model Height (m)
1	5930	17	140	33	6360
2	5350	18	910	40	1710
3	4280	19	1490	41	1610
4	6610	20	1010	42	1680
5	2730	21	1130	43	110
6	5070	22	1220	44	780
7	4700	23	1240	46	2480
8	4940	24	160	51	5970
9	5140	25	4290	52	5140
10	5050	26	4010	53	5030
12	4010	27	4190	54	5270
13	700	28	4650		
14	0	30	6450		
15	310	31	5210		
16	240	32	440		

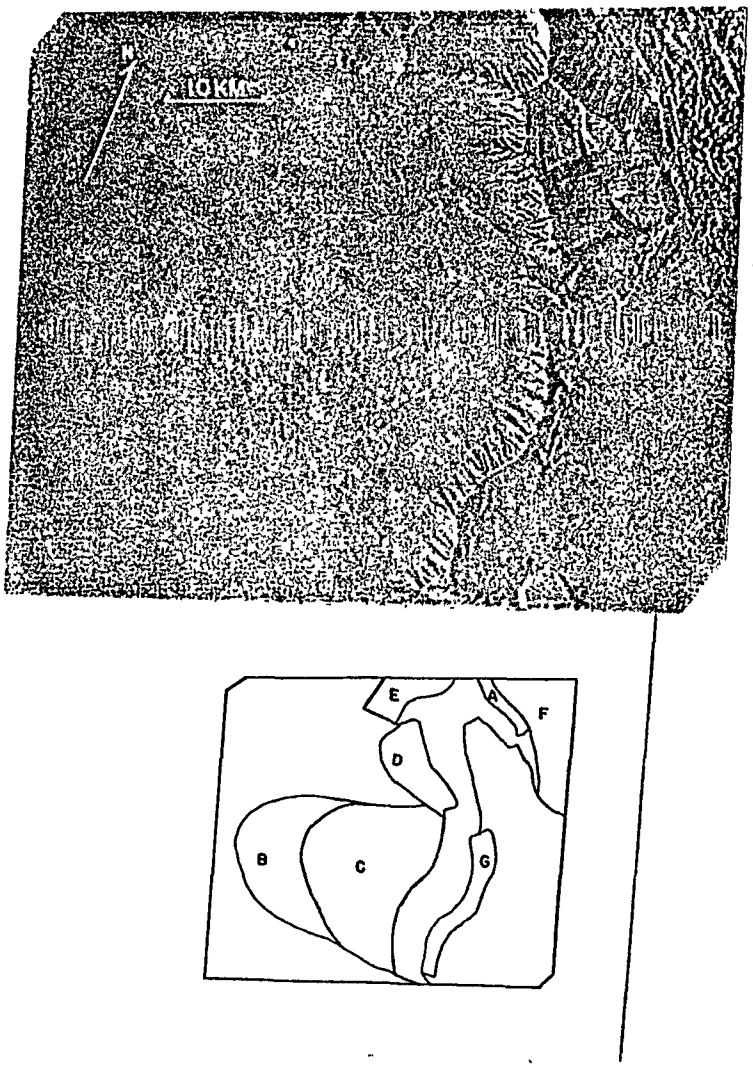

Figure 7. Enhanced photo (DAS 6823743) of the south end of the west reach of Olympus Mons' basal scarp. Line drawing is a key to terrain features discussed in text.

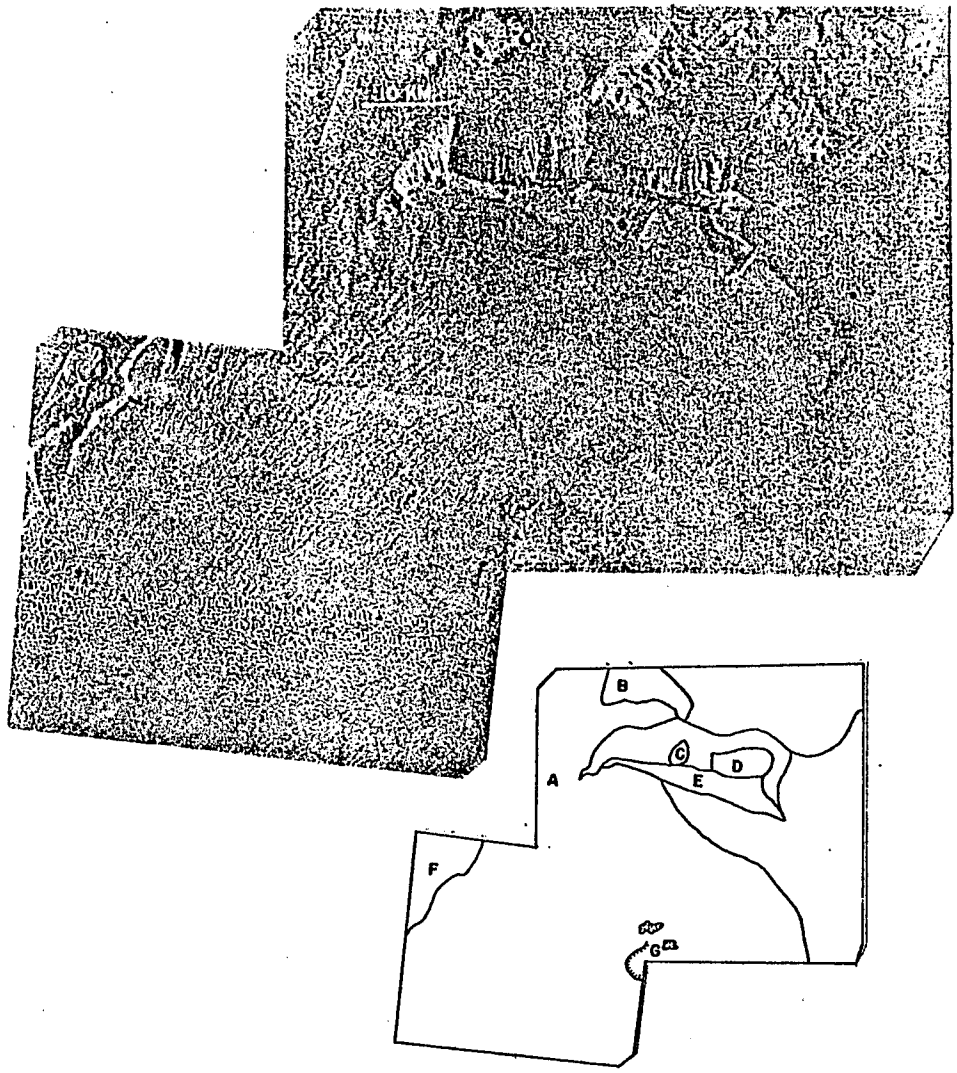

Figure 8. Mosaic of enhanced photos (DAS 6823948, 9701239) of part of Olympus Mons' lower north flank and basal scarp. Line drawing is a key to terrain features discussed in text.

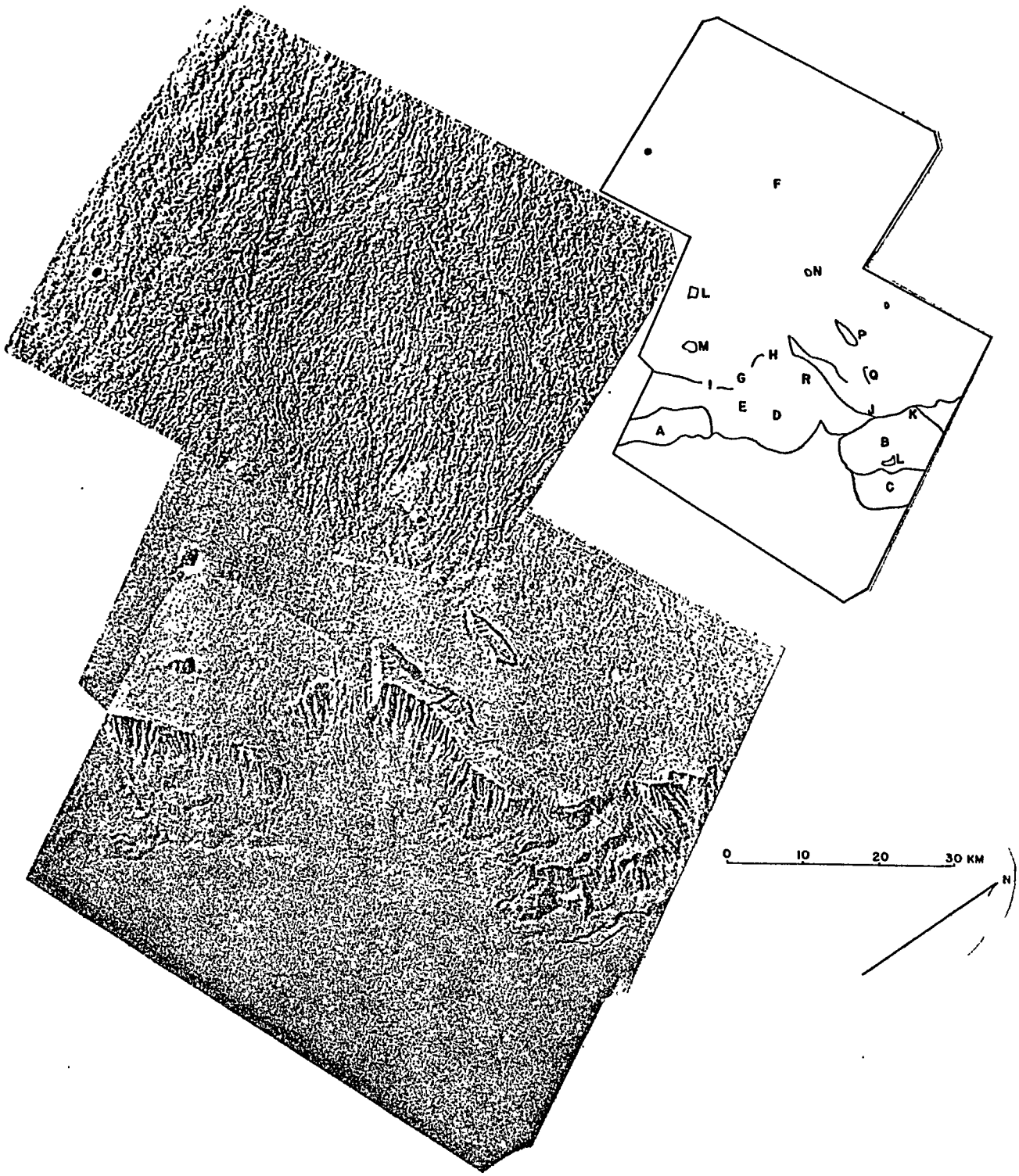

Figure 9. Mosaic of enhanced photos (DAS 6895698, 9845299, 9845369) showing part of Olympus Mons' southeast flank and basal scarp. Line drawing is a key to terrain features discussed in text.

the west base of Olympus Mons. Some of these rough areas have a lobate form and extend as much as 35 km from the base of the escarpment. Two such lobes are clearly shown at the southwest margin of Olympus Mons on a high resolution photo (Fig. 7).

Locally to the north "grooved terrain" (McCauley et al., 1972) comes to the foot of the basal scarp (Fig. 8). The contact is abrupt, involving a marked change in surface texture and an apparent sharp break in slope.

ROCKSLIDES

The areas of rough, irregular jumbled terrain along the west reach of scarp resemble deposits formed by some terrestrial landslides, particularly large-scale rockslides and rockfalls. According to Sharpe (1938, p. 64, 76, 78):

> ....(a landslide is) the perceptible downward sliding or falling of a relatively dry mass of earth, rock, or mixture ot the two.
>
> ....(a rockslide is) the downward and unusually rapid movement of newly detached segments of bedrock sliding on bedding, joint, or fault surfaces or any other plane of separation.
>
> ....(a rockfall is) the relatively free falling of a newly detached segment of bedrock of any size from a cliff, steep slope, cave or arch.

Since the exact mode of motion of possible martian landslides cannot be known, the term "rockslide" will denote here landslides which were perhaps similar to terrestrial rockslides or rockfalls.

Characteristics

The several lobate areas of irregular terrain extending 10 to 20 km from the foot of the west basal scarp (Figs. 3 and 4) with widths of 10 km to 25 km have hills and ridges arranged in increasingly orderly patterns toward the margins and distal end. These marginal ridges and scarps are roughly conformal with the shape of the lobe, somewhat like recessional glacial moraines.

The largest lobe (B and C in Fig. 7) is about 25 km wide and 30 km long. The four most prominent conformal ridges near its terminus are 2 to 5 km apart near the axis of the lobe but converge as they curve back along the margins. These ridges have rounded summits and gently sloping flanks which merge with the smooth floored hollows. The total number of conformal ridges is probably not resolved by Mariner 9 photos.

Inside the zone of conformal ridges lies mostly irregularly hummocky terrain (C in Fig. 7) covering an area about 23 km long and 20 km wide. Principal features are small mounds 300 to 1000m across, and ridges and scarps, up to 7 km long, which are only roughly conformal with the lobe margin. A small circular depression about 1 km across may be an impact crater.

Immediately to the north is a second and smaller lobe (D in Fig. 7) about 15 km wide and 9 km long. A 3 km long terminal ridge and a parallel scarp 500 to 1000m behind it

are the only visible conformal topographic features, the remainder of the lobe resembling the interior of the larger lobe. Part of a third area of similar irregular terrain appears just north of this smaller lobe (E in Fig. 7). This patch of hilly terrain approximates 100 km^2 in area and is bounded to the east and north by large spurs projecting from the basal scarp (Figs. 3 and 7). This mass is not lobate, for the south and west margins are defined by two linear outward facing slopes which meet at an angle of about 90°.

Other high resolution images along the base of Olympus Mons do not reveal similar lobes of irregular terrain, but four additional areas of possibly similar terrain are identified along the west basal scarp (G and H in Fig. 4) in low-resolution photos. These areas are vaguely lobate and similar in size.

Speculations on Origin

Lobes of hilly terrain are interpreted as rockslide or rockfall deposits because of their form, topography and location at the base of a large escarpment, which shows signs of continued failure. Small troughs and scarps extending approximately 4 km back from the brink of the basal scarp, and trending parallel to it (G in Fig. 7), suggest incipient scarp failure.

Mudge (1965) enumerates the following distinctive geomorphic features of terrestrial rockfall and rockslide deposits:

> (1) hummocky surface; (2) relatively low relief from head to toe; (3) arcuate ridges and furrows, at least where confined; (4) lobate form (where not confined); (5) local pressure ridges where flowage was impeded by barriers; (6) trough between head of the deposit and the base of cliff or scar; (7) movement up or over topographically high ground; and (8) volume measurable in millions of cubic yards of rock.

Martian lobes are generally hummocky, relatively low in relief, possess arcuate ridges, have lobate form and have probable volumes of many millions of cubic yards. The seeming lack of a trough between the hummocky terrain and the base of the escarpment may be due to photographic limitations or subsequent accumulation of talus. Lobes of hilly terrain differ from most terrestrial slide deposits in size and internal topography. The largest lobe is more than twice the length of the two largest known terrestrial slides (Mudge, 1965). Only a few terrestrial slide deposits have an interior jumbled topography with increasingly orderly patterns towards their distal ends and margins.

The extraordinary length of the largest martian slide deposit may be attributed to a low rate of energy loss by sliding friction and a large gravitational energy input from descent of the 4 km basal scarp. Quantatative comparison with large terrestrial slides can be made using data compiled by Mudge (1965), Shreve (1966, 1968), and Howard (1973). A measure of sliding efficiency is a landslide's "coefficient of friction", defined as the maximum elevation drop divided

by the overall length of the slide deposit. Parameters of the largest martian slide yield a friction coefficient of 0.11, close to the exceptionally low values of four large terrestrial rockslides (Howard, 1973). Shreve (1968) proposes a mechanism for greatly reducing sliding friction of some landslides to account for low friction coefficients. He suggests that large rockfalls are able to trap and slide upon a cushion of compressed air.

Trapped Air Cushion Hypothesis

Conformal ridges near the terminus of a slide lobe are considered by Shreve (1968) to be diagnostic of lubrication by a trapped cushion of air. When the layer of air trapped beneath a slide mass has thinned sufficiently by spreading and leaks from the slide margins the mass comes to rest in stages producing a characteristic topographic pattern. The features of this pattern large enough to be seen in Mariner IX images are:

1. Lateral ridges formed when air leaking from beneath the more slowly advancing lateral margins allows a strip of material to settle while the central part of the slide continues to move and thin.
2. A distal rim and scarp are formed as air leakage from beneath the advancing margin of the slide causes it to settle to a sudden halt so that sliding debris piles up behind.

3. Transverse ridges form in succession backwards from the grounded front. Successive piling up and thrusting sliding material produces an imbricate internal structure and surficial transverse ridges.

A wave of impact may also travel forward through a sliding sheet forming a pattern of transverse fissures, but these features are probably much smaller than the resolution limit ($\sim$ 300m) of Mariner IX images.

An implied low coefficient of friction and a distinctive surface morphology suggest that the Olympus Mons debris lobes may have been lubricated by trapped gas. From observations of large slides in motion and the topography of the Blackhawk Slide in the San Bernardino Mountains of southern California, Shreve (1968) estimated that a layer of compressed gas averaging 1 foot thick underlay the Blackhawk Slide as it came to a halt. Trapping of such a layer of air under martian slides seems unlikely in view of the present low atmospheric pressure. Ridges and hills in the interior of the largest martian slide are probably a minimum of 100m high, (a qualitative estimate from Fig. 7). In order to form these features by piling up and overthrusting, the original sliding sheet had to be at least 20 m thick. If its density was 2 gm/cm^3 then pressures beneath the moving debris were 320 times the normal martian surface pressure of 5 mb. Allowing for adiabatic compression, the landslide would have had to trap 17 km^3 of

atmosphere to form a layer of compressed gas 1 foot thick and 840 km^2 in area. The segment of escarpment from which the slide originated is no more than 22 km long, so in cross section the slide mass would have had to override an average of at least 0.8 km^2 of atmosphere while descending about 4 km. This seems unlikely since the only obstacle which might have launched the slide mass into the air is a probable 10° break in slope between the upper and lower faces of the escarpment.

If the volume of the rockslide is less than estimated, less gas might suffice to cushion its motion. Although the estimation of thickness is admittedly crude, a total slide volume of about 17 km^3 seems reasonable. A block of that volume and 22 km in length would have a cross sectional of about 0.8 km^2. Linear features suggestive of incipient scarp failure are seen in a zone 4 km wide at the top of the scarp (G in Fig. 7), so the collapse of 17 km^3 of material is not improbable.

Alternative Hypotheses

If large Martian rockslides cannot currently be adequately lubricated by a cushion solely of trapped atmospheric gas, two alternative sources of gas are:

1. Adsorbed gases released from slide material while it is in motion.
2. A denser Martian atmosphere in the past.

Carbon dioxide physically adsorbed on Martian surface materials may be abundant enough to contribute significantly to the lubrication of landslides. Fanale and Cannon (1971) showed that pulverized basalt at typical Martian surface pressures and temperatures can adsorb large quantities of CO_2. At -50°C and 6 mb pressure (reasonable conditions in the shallow Martian subsurface) the pulverized rock adsorbed 270 times its own volume. A 1 km layer could store 400 gm/cm^2 of CO_2 (Fanale, 1973, private communication), far exceeding the amount in the present atmosphere. Materials exposed in the face of Olympus Mons' basal scarp might have a similar adsorption capacity. Fifteen joules per gram of gravitational energy, acquired in a fall of 4 km, would be sufficient to raise the temperature of typical silicate rocks (specific heat 0.2 cal/gm-°C) about 17.5° and drive off some gas. Isothermic adsorption data at 29°, 0°, and -77°C (Fanale and Cannon, 1971) indicate a very steep rise in adsorption at the lowest temperature, so it may be possible to release a significant fraction of adsorbed CO_2 with a modest temperature change of 10 to 20°. Heat of adsorption would be an additional energy sink during disequilibrium release of adsorbed CO_2 in a landslide. Heats of adsorption, though not experimentally well determined, are typically 2 to 5 kcal per mole, less than 5 percent of the estimated gravitational energy released in a 4 km fall. Data now available are insufficient to estimate the quantity of CO_2

which might be released, but they suggest the possibility that dry Martian slides provide some of their own gaseous lubrication. Released CO_2 may be of sufficient quantity to convert a dry slide mass into a highly mobile gas suspension.

If Mars formerly possessed a denser atmosphere, an atmospheric gas cushion might account for the observed characteristics of Martian rockslide deposits. Sagan, et al., (1973) have proposed that advective instability of the Martian atmosphere creates two stable climatic regimes - one with low surface pressures as at present and one with much higher pressures, utilizing solid CO_2 stored in the permanent polar caps. Variations in the obliquity of Mars with a period of about 10^5 years (Ward, 1973) may be capable of driving this instability. Alternatively, oscillations in obliquity may raise atmospheric pressure by periodically distributing more insolation on the polar caps (Ward, 1974 and Ward, Murray, and Malin, 1974). Different estimates of the mass of the solid CO_2 reservoir on Mars yield potential peak surface pressures in the range 15 to 30 mb (Murray and Malin, 1973) to 1 bar (Sagan et al., 1973). Within the more conservative range of estimated peak pressures, the volume of trapped atmosphere needed to cushion the largest rockslide is estimated at 5 to 8 km^3 (assuming a slide thickness of 20 m). These volumes of trapped gas are very large but not completely unreasonable for a slide

from a scarp 22 km long and 4 km high.

SLUMP

North and southeast reaches of the basal scarp have a benched form of a type created by slumping. Similar forms on terrestrial escarpments are attributed to slump. Sharpe (1938, p. 65) describes a slump as:

> ....the downward slipping of a mass of rock or unconsolidated material of any size, moving as a unit or as several subsidiary units, usually with backward rotation on a more or less horizontal axis parallel to the cliff or slope from which it descended.

Characteristics

The basal scarp of Olympus Mons locally displays two or more outward facing steep slopes separated by flat to gently sloping surfaces. At high resolution some of the steep faces can be seen to be fluted. At the north margin of Olympus Mons benched forms extend laterally 50 km along the basal scarp and a similar distance out from its brink (Fig. 4). Most benched parts of the north basal scarp are seen only in low resolution images (Fig. 3). Two areas of about 600 and 200 km^2 (J and K in Fig. 4) each display three secondary scarps spaced 5 to 10 km apart.

Two individual benches, (1 in Fig. 4) are identified only from a high resolution photograph (Fig. 8). They are situated slightly below the brink of a distinct 50 km reach of basal escarpment (C and D in Fig. 8). Unlike the surface above the basal scarp the bench surfaces appear rough at a

scale of 1 km and less.

Two other areas shown in Figure 8 have features which resemble slumps. The cratered and faulted surface above the basal scarp (E in Fig. 8) forms a large bench apparently sloping backward into the lava covered volcano flank. The contact between the two surfaces is strikingly linear and appears to mark an abrupt break in slope. A scarp at the west end of this bench (F in Fig. 8) dies out to the south beneath a mantle of lava flows.

A small part of a north-south zone of disrupted volcano flank (F in Fig. 4) is shown at F in Figure 8 where it is composed of broad ($\sim$ 5 km wide) benches. Some bench surfaces show lava flow patterns which are broken by marginal scarps.

At the southeast margin of Olympus Mons are two intervals of benched escarpment 70 and 100 km long and 10 to 25 km wide, (L and M in Fig. 4). Benches typically number 2 to 4 and are 4 to 10 km wide. The 100 km long shadowed eastward facing reach of the basal scarp just to the north (Fig.3) may also be benched: some faint linear markings parallel the trend of the scarp.

High resolution images of southeast basal scarp (Fig.9) show relationships which suggest mantling of a preexisting blocky terrain by lava flows. Parallel ridges and troughs can be traced downslope from lava flow terrain high on Olympus Mons' flank (F in Fig. 9) and over the brink of the basal scarp. At G and E in Figure 9 these features appear to be

diverted around a sharp promontory. Parallel ridges and troughs cross the escarpment brink at G and H at the head of a lobe (D in Fig. 9) about 15 km wide, which mantles the basal scarp face and extends out about 7 km onto the basal plain. Faint subparallel downslope trending ridges are discernible on the surface of the lobe. At I, J, and K in Figure 9 the apparent flow features cross the brink of the escarpment and descend onto benches. Directly below I and K benches appear to have been partially buried. Below J and K (in area B of Fig. 9) it appears that flow of material, as evidenced by low ridges, was directed along bench surfaces parallel to the trend of the escarpment. Most of the scarp faces between benches appear unmantled, suggesting that backward tilt of original surfaces channeled flowing material parallel to the secondary scarps. One small bench surface (L in Fig. 9), which has no linear features suggestive of mantling, slopes distinctly backward into the basal escarpment. Trends of linear features on the lower flank of Olympus Mons also suggest diversion of flowing material around several elevated blocks (L, M, N, P, Q in Fig. 9).

Bench forms extend out onto the plains at the foot of the southeast basal scarp (C in Fig. 9). Small scarps there parallel the trend of the escarpment and have a spacing similar to that of the scarps between benches.

Speculations on Origin

Most of the benched forms on segments of Olympus

Mons' basal scarp are interpreted as the product of gravity slumping. Blocks appear to have moved downslope with little internal disruption, their outward faces in some locations retain characteristics of the original basal scarp face. Backward rotation of blocks is suggested by the inclination of bench surfaces.

Other benches seen along the north basal scarp may not have been caused by simple gravity slumping. The large bench at E in Figure 8 may be a remnant of a once more extensive surface across which the margin of the growing volcano has advanced. Unlike other presumed slumps no break-away scarp is seen above this large feature.

Benches along a north-south trending zone of disrupted volcano flank, F in Figure 8, are separated by scarps which trend generally downslope. Tensional stresses required to produce such scarps must have been directed approximately east-west, orthogonal to the gravitational stresses on the slope. One possible origin for this zone of disruption is local subsidence, perhaps due to withdrawal of magma at depth. A cluster of three craters (G in Fig. 8), two of them complex in form, suggests prolonged activity of a major volcanic vent in this area. Alternatively the disruption may have been caused by east-west tensional regional stresses. Steep-faced N to NNE trending linear scarps just north of Olympus Mons (in area L2 of Fig. 4) suggest major crustal faulting extending south into the

north end of this zone of disruption.

Some slumping apparently occurred before some of the more recent eruption episodes of Olympus Mons. On southeast basal escarpment (Fig. 9) features interpreted as lava flows mantle some bench surfaces and break-away scarp faces. Flows are also diverted around elevated blocks, possibly remnants of slump masses, on the lower flank of the volcano.

Low impact crater densities indicate that the volcano flank from which flows extend to mantle the southeast basal scarp are among the youngest areas of lava flow terrain photographed at high resolution on Olympus Mons (Blasius, 1975). This area has less than one-fourth the density of probable impact craters observed near the volcano's summit.

The integrity of slump blocks indicates that scarp materials in the slumped areas along the southeast and north basal scarps, are relatively competent. If ground ice is ubiquitous and its decay is responsible for other types of mass movement along the basal scarp (see IRREGULARLY LINEATED TERRAIN), then either ground ice has not decayed in the areas of slump or materials there are inherently more competent.

Slump features and other evidence suggest that the southeast basal scarp of Olympus Mons was formed by vertical crustal displacements. Lobes of grooved terrain, which form

an aureole about Olympus Mons (L1 to L6 in Fig. 4), appear to have been tilted generally toward the volcano (Carr, 1973). Two lobes east and southeast of Olympus Mons appear to be similarly tilted, to the northwest. The extension of slump features beyond the southeast basal scarp (C in Fig. 9) suggest uplift of the volcano margin or subsidence of adjacent plains. A northeast trending zone of subsidence would account most simply for both the existence of the southeast basal scarp and the tilt of blocks of grooved terrain.

IRREGULARLY LINEATED TERRAIN

A third type of terrain seen along the basal scarp of Olympus Mons may have been formed by a mass movement process. From its general appearance, this terrain is described as "irregularly lineated."

Characteristics

Irregularly lineated terrain occurs within two similar sized areas, totaling about 8000 km^2, on the west margin of Olympus Mons (C and D in Fig. 4). There, for distances of 80 and 100 km, the basal scarp is subdued and characterized by irregular ridges, troughs, and scarps, for the most part aligned subparallel downslope. At its upper margin lineated terrain joins the smooth lower flank of Olympus Mons transitionally; topographic forms decrease in size abundance and increase in irregularity until they fade below

image resolution.

A small fraction, about 200 km^2, of the larger southern area (D in Fig. 4) was photographed at high resolution (F in Fig. 7). Some of the middle and upper parts of this area and the bounding escarpment on the south are seen. Ridges, troughs and elongate tilted smooth surfaces, aligned predominately downslope, comprise this segment of lineated terrain. These features individually range up to 2 km wide and 8 km long. At higher levels alignments become more irregular and individual linear features shorter. A transitional zone between lineated terrain and smooth volcano flank consists of more or less equant patches of smooth surface bounded by low scarps and troughs. The largest of these patches are about 3 km across. The boundary between the smooth lower face of the bounding escarpment (A in Fig. 7) and the lineated terrain is a sharp break in slope.

The lower part of the southern area of irregularly lineated terrain consists of subdued downslope trending ridges and troughs (Fig. 3). These mostly fade below photo resolution 30 to 90 km downslope from the margin of smooth volcano flank. Some of the largest ridges, up to 50 km long and 6 km wide, seem to have lobate terminations.

The character of the basal scarp within areas of lineated terrain ranges from slightly to greatly subdued and is in striking contrast to the scarp on either side. The larger

southern area (D in Fig. 4) forms a re-entrant into the basal scarp which is bounded north and south by prominent nearly linear escarpments which die out upslope. The northern area of lineated terrain (C in Fig. 4) shows some similarities to the southern area, but the features are not as well developed and photo resolution is poorer. The basal scarp of the volcano is topographically less subdued and only the north margin of this area is bounded by a prominent escarpment.

Speculations on Origin

The subdued and embayed character of the basal scarp in areas of irregularly lineated terrain suggest that it is an erosional terrain. Fluvial erosion or mass movement are most compatible with the downslope trends of ridges and valleys. The lack of any pattern of connected channels within the lineated terrain suggests that postulated erosion was accomplished by broad mass movement of slope materials rather than cutting by streams. Patches of undisrupted surface which occur in upper lineated terrain indicate that not all areas were equally affected. The location of lineated terrain on the flank of a great volcano suggests that mass movement has been initiated in some way by the heat or gaseous products of volcanism. The decay of ground ice and the chemical alteration of rock are two processes which might both weaken slope materials and provide lubricants (water and clays) for mass movement.

An alternative explanation, which seems less attractive, is that lineated terrain is volcanic in origin, perhaps being made up of an upper collapsed part owing to subsurface magma withdrawal, and a lower part where lava flows were erupted. Evidence of subsidence in volcanic regions is widely present on Mars in the form of calderas on volcanic constructs (as in Fig. 3). Calderas are generally bounded by simple scarps which are oval in plan, very different in character from the irregular zone of blocks, scarps, and troughs along the upper margin of lineated terrain. The subdued ridges in the lower levels of lineated terrain do not resemble lava flows as seen elsewhere on Olympus Mons. In the low resolution mosaic of the volcano (Fig. 3) the ridges of lineated terrain stand out prominently as high contrast features while the largest lava flows identified in a high resolution photo (Fig. 9, top), are undetectable at low resolution. The ridges of lineated terrain have considerable greater vertical relief than the largest flank lava flows. It might be argued that the style of volcanism represented by lineated terrain is different from that which built most of Olympus Mons. It seems improbable, however, that this activity would be confined to just the western basal scarp.

If the upper levels of irregularly lineated terrain are the product of erosion, there should be a corresponding area of accumulation of eroded material. The long ridges

of lower lineated terrain may be deposits of individual mass flowage events, and materials may also have been spread widely over the smooth plain at the base of Olympus Mons.

TALUS

Along with the large-scale mass movements discussed, talus accumulation from small rockslides and falls probably also takes place. As described in the INTRODUCTION, the steepest sections of simple basal scarp have fluted upper faces and smooth less steep lower faces. In some locations the lower scarp face appears to be made up of adjacent conical segments. The flutes vary little in width from top to bottom and begin at the brink of the scarp. These characteristics suggest an origin as avalanche chutes (Blackwelder, 1942). Aprons and cones of talus probably form the smooth slopes below.

CONCLUSIONS

Three types of large-scale mass movement phenomena -- rockslides, slump, and a type of mass flowage have been tentatively identified from landforms seen along Olympus Mons' basal escarpment. In addition, debris or avalanche chutes and accumulated talus are probably widely present along steeper sections of basal scarp.

Different reaches of the basal escarpment differ greatly in character and in the types of mass movement that have

occurred along them. The west basal scarp is deeply embayed, suggesting considerable retreat. Indications of large rockslides and mass flowages are seen only along this reach, so these events may be important mechanisms of scarp recession.

The southeast basal scarp is made up of long straight reaches which, for the most part, have a benched form suggestive of slumping. Low scarps beyond the foot of the basal escarpment and the apparent tilt of crustal blocks to the east and southeast of Olympus Mons suggest that the southeast basal scarp was formed by subsidence or downwarping along the margin of the volcano.

The north basal scarp is intermediate in character. It is deeply embayed like the west basal scarp, but the only evidences of large-scale mass movements are several short reaches of benched escarpment probably formed by slump. The difference in character from the west basal scarp may be due to essentially different erosional mechanisms or to their scale, rockslides and mass flowages having been smaller and not detectable in low resolution photos of the north basal scarp.

Lava flows which mantle sections of north and southeast basal scarp indicate that Olympus Mons' basal scarp did not develop simply by erosion of an extinct volcanic shield. Instead, the basal scarp represents an interplay between constructional volcanic processes, tending to extend the volcanic shield, and erosional and tectonic processes

tending to diminish it.

Blackwelder, E., 1942, The Process of Mountain Sculpture by Rolling Debris: J. of Geomorphology, v.5, p.325-328.

Carr, M.H., 1973, Volcanism on Mars: J. Geophysical Res., v.78, p.4049-4062.

Carr, M.H., Masursky, H., and Saunders, R.S., 1973. A Generalized Geologic Map of Mars: J. Geophysical Res., v.78, p.4031-4036.

Christensen, E.J., 1974, private communication, Mars topographic Map.

Fanale, F.P. and Cannon, W.A., 1971, Adsorption on the Martian Regolith: Nature, v.230, p.502-504.

Howard, K.A., 1973, Avalanche Mode of Motion: Implications From Lunar Examples: Science, v.180, p.1052-1055.

McCauley, J.F., 1973, Mariner 9 Evidence for Wind Erosion in the Equatorial and Mid-Latitude Regions of Mars: J. Geophysical Res., v.78, p.4123-4138.

McCauley, J.F., Carr, M.H., Cutts, J.A., Hartmann, W.K., Sharp, R.P., and Wilhelms, D.E., 1972, Preliminary Mariner 9 Report on the Geology of Mars: Icarus, v.17, p.289-327.

Mudge, M.R., 1965, Rockfall-Avalanche and Rockslide-Avalanche Deposits at Sawtooth Ridge, Montana: Geological Society of America Bulletin, v.76, p.1003-1014.

Murray, B.C. and Malin, M.C., 1973, Polar Wandering on Mars?: Science, v.179, p.997-1000.

Sagan, C., Toon, O.B., and Geirasch, P.J., 1973, Climatic Change on Mars: Science, v.181, p.1045-1049.

Sharpe, C.F.S., 1938, Landslides and Related Phenomena: Morningside Heights, New York, Columbia University Press, 137p.

Shreve, R.L., 1966, Sherman Landslide, Alaska: Science, v.154, p.1639-43.

Shreve, R.L., 1968, The Blackhawk Landslide: Geological Soc. of America Special Paper 108, 47p.

References - (continued)

Ward, W.R., 1973, Large Scale Variations in the Obliquity of Mars: Science, v.181, p.260-262.

Ward, W.R., 1974, Climatic Variations on Mars: I. Astronomical Theory of Insolation: J. Geophysical Res., v.79, p.3375-3386.

Ward, W.R., Murray, B.C., and Malin, M.C., Climatic Variations on Mars: 2. Evolution of Carbon Dioxide Atmosphere and Polar Caps: J. Geophysical Res., v.79, p.3387-3395.

Wu, S.S.C., Schafer, F.J., Nakata, G.M., Jordan, R., and Blasius, K.R., 1973, Photogrammetric Evaluation of Mariner 9 Photography: J. Geophysical Res., v. 78, p. 4405-4423.

III. A STUDY OF MARTIAN TOPOGRAPHY BY ANALYTIC PHOTOGRAMMETRY

A Study of Martian Topography by Analytic Photogrammetry[1]

KARL R. BLASIUS

Division of Geological Sciences, California Institute of Technology
Pasadena, California 91109

Many overlapping pictures, potential data for the construction of topographic maps, were obtained by the television cameras on Mariner 9. An analysis of the sources of error in photogrammetric determinations of relief from these pictures singles out photo resolution as the primary limiting factor. Topographic maps of several Martian surface features, derived by an original analytic scheme, are presented. The observed errors in relief determinations using this technique are in good agreement with the independent error analysis.

When the television experiment for the Mariner Mars 1971 Project was planned, the stereometric potential of the television cameras was ignored in favor of scientific objectives that required only single pictures or multiple coverage without a requirement of different viewing perspectives [*Masursky et al.*, 1970].

However, as the mission developed, with one spacecraft instead of two and with a severe dust storm obscuring surface features, a reevaluation was required, and much day-to-day improvisation was necessary. As a result, early in the mission we obtained significant multiple photographic coverage of the few surface features that were relatively clear of intervening dust. In the equatorial regions of Mars four of these features proved to be great volcanic shields with local relief of the order of tens of kilometers. This discovery, coupled with the availability of many overlapping pictures, made photogrammetry from Mariner 9 pictures an exciting possibility.

While the mission was still in the planning stage, it was realized that the potential for photogrammetry might exceed original expectations, so an analytic routine was prepared to test the quality of any potential stereo pairs for determining relative relief of point features seen in two pictures taken from sufficiently different camera stations (see the appendix). This technique now has yielded several stereo models of surface features of great geologic interest and has demonstrated the potential of the Mariner 9 pictures for construction of contoured topographic maps through the use of stereo plotters. This latter work is in progress, and its first results are now being published [*Wu et al.*, 1973]. This paper discusses the photogrammetric potential of Mariner 9 data and the analytically determined topography of certain Martian landforms.

Precision of Relief Measurement

The photographic phenomenon that allows height measurement from photography is termed relief displacement. Referring to Figure 1, in which an object **H** of height H imaged by a camera of focal length f is represented, we see that the image of the top of **H** is formed at a point farther from the nadir image N' than is the image at the foot of **H**. The distance H' between these two image points is the relief displacement of the top of **H** due to its elevation. If **H** is imaged within a small angle of the camera axis (a very good approximation for the Mariner cameras, whose angular fields are only 1.1° × 1.4° and 11° × 14°), these quantities are approximately related by the equation

$$H = H'/\sin(VAR)SR/f \qquad (1)$$

where SR is the slant range of the camera from the feature and VAR is the viewing angle at the feature measured from the local vertical. If we take partial derivatives of (1), we obtain an equation for small changes, ΔH, in any

[1] Contribution 2250, Division of Geological Sciences, California Institute of Technology, Pasadena, California.

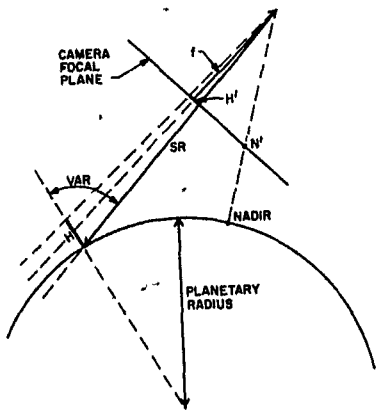

Fig. 1. Basic elements of the geometry of an oblique planetary scale picture in the principal plane (the plane containing the nadir and the camera axis).

relief determination in terms of small changes in the other quantities:

$$\Delta H = C_0\Delta H' + C_1\Delta f + C_2\Delta SR + C_3\Delta VAR \qquad (2)$$

where

$$\begin{aligned} C_0 &\equiv SR/[f\cdot\sin(VAR)] \\ C_1 &\equiv -H'/\sin(VAR)\,SR/f^2 \\ C_2 &\equiv H'/\sin(VAR)1/f \\ C_3 &\equiv [-H'\cdot\cos(VAR)]/\sin^2(VAR)\,SR/f \end{aligned} \qquad (3)$$

The quantities whose variations are shown in (2) to contribute to ΔH fall into two distinct categories according to their effect on a stereo model. Many determinations of H' go into the construction of a single stereo model, and so random errors in the measurement process may appear as inconsistencies in the derived topography (see the appendix). Errors in f, SR, or VAR, on the other hand, create an overall model scaling error. We shall find that predicted random errors in H' account well for the inconsistencies observed in the stereo models and should dominate the effects of errors in f, SR, and VAR in wide angle Mariner 9 photography.

For a sample error analysis consider the simple case where one picture of a pair was taken from an oblique perspective (the case of Figure 1) and the other was taken from a vertical perspective ($VAR = 0$). In Table 1 typical values of the parameters of (1) are given for the members of such a Mariner 9 picture pair. The uncertainties in some of the quantities on the right-hand side of (1) can be estimated from work performed by JPL scientists. Preflight calibration data [*Snyder*, 1971] gives 1-σ uncertainties in the focal lengths as listed in Table 1.

In creating a self-consistent stereo model (see the appendix) the slant range SR may have to be changed from the nominal value for one of the pictures, and so the unchanged SR of the other picture sets the scale for the model. The basic quantities involved in calculating SR are the radius of the planet R, the range to the center of the planet $RMAG$, and the tilt angle of the camera axis away from the direction to the center of the planet. For the small tilt angles of our examples (less than 20° for the oblique pictures) the probable error in SR, ΔSR, is due to ΔR and $\Delta RMAG$. Both preflight and post-flight analyses agree that there is a 5-km (1-σ) uncertainty in calculated values of $RMAG$ at periapsis (E. J. Christensen, personal communication, 1972). This error scales approximately as a constant percentage of $RMAG$. For the largest values of $RMAG$ that affect our models, we find $\Delta RMAG = 8$ km.

Estimating Mars' radius at any location is a very subjective matter, since preliminary and scattered data must be combined from several sources, such as Mariner 9 occultation and spectrometer experiments and earth-based radar data. On the basis of such an informal procedure, we estimate a probable error of 5 km in the assumed values of Mars' radius. In combination with the value of $\Delta RMAG$ given above, we find $\Delta SR \simeq 10$ km.

A Jet Propulsion Laboratory (JPL) study of the precision of the spacecraft pointing angles from the positions of ground features in repeated photography (S. Mohan, personal communication, 1973) concluded that they were generally accurate to better than 0.1°. This

TABLE 1. Typical Values of Photogrammetric Parameters Associated with Mariner 9 Pictures of Martian Surface

Camera	SR, km	$f(\pm 1\,\sigma)$, mm	VAR, deg	H, km	H' Derived by Using (1), mm
Wide angle	2×10^3	52.267 (±0.006)	30	5	6.25×10^{-2}
Narrow angle	2×10^3	500.636 (±0.036)	30	5	6.25×10^{-1}

translates into a ΔVAR of ab
photo of our sample stereo r
were not taken from extre
extremely oblique perspectives.
for a model, if the errors are a
correlated, is then approximate

The uncertainty in H' is r
curacy with which the distan
features can be determined in
plane. Two factors are involvec
resolution of the cameras ar
fidelity of the processed pictu
single figure for spatial reso
characteristic is a function o
the target scene. A discussion
in connection with photogra
craft is contained in a recent
et al., 1970]. For this error
spatial resolution of 0.027 m
to a high-contrast target such
crater illuminated by a sun lo
point features to be located a
such resolved features. This
an accuracy of 0.007 mm. (T
chosen to construct the stereo
later in this paper closely
ideal.) The derivation of one
the location of four image poin
of features in two pictures. Th
from the difference in the ima
tween that pair of features.

The geometric fidelity of t
complicated problem that invo
measurement of electronic and
created by the cameras and th
returned pictures. A detailed
procedure is now in preparat
unpublished manuscript, 1973)
calibration routine a square g
used. Accurate determinations
of about 400 intersections on
compared with their coordin
metrically corrected image of
believed that there are seve
sources of systematic, but sma
image coordinates.) For both M
the rms separation of the ac
positions from their images is les
(J. Kreznar, personal communi
we assume that this figure can l
Mariner 9 pictures generally, we
probable error for a single point

translates into a ΔVAR of about 0.1° for each photo of our sample stereo model, since they were not taken from extreme altitudes or extremely oblique perspectives. The total ΔVAR for a model, if the errors are assumed to be uncorrelated, is then approximately 0.15°.

The uncertainty in H' is related to the accuracy with which the distance between point features can be determined in the camera focal plane. Two factors are involved here: the spatial resolution of the cameras and the geometric fidelity of the processed pictures. There is no single figure for spatial resolution, since this characteristic is a function of the contrast of the target scene. A discussion of this problem in connection with photography from spacecraft is contained in a recent paper [*Masursky et al.*, 1970]. For this error analysis I use a spatial resolution of 0.027 mm corresponding to a high-contrast target such as a steep-walled crater illuminated by a sun low in the sky. The point features to be located are the centers of such resolved features. This is easily done to an accuracy of 0.007 mm. (The point features chosen to construct the stereo models presented later in this paper closely approximate this ideal.) The derivation of one elevation requires the location of four image points, the same pair of features in two pictures. Then H' is derived from the difference in the image distances between that pair of features.

The geometric fidelity of the pictures is a complicated problem that involves the preflight measurement of electronic and optical distortions created by the cameras and their removal from returned pictures. A detailed discussion of this procedure is now in preparation (J. Kreznar, unpublished manuscript, 1973). In part of the calibration routine a square grid of lines was used. Accurate determinations of the coordinates of about 400 intersections on that grid can be compared with their coordinates on a geometrically corrected image of the grid. (It is believed that there are several uncalibrated sources of systematic, but small, errors in the image coordinates.) For both Mariner 9 cameras the rms separation of the actual intersection positions from their images is less than 0.004 mm (J. Kreznar, personal communication, 1972). If we assume that this figure can be applied to the Mariner 9 pictures generally, we can estimate the probable error for a single point feature position determination $\Delta P'$ by combining the effects of picture resolution and geometric distortion:

$$\Delta P' \approx [(0.007)^2 + (0.004)^2]^{1/2} = 0.008 \text{ mm} \quad (4)$$

Picture resolution is the dominant source of error here. The uncertainty in H', due to four such determinations, is estimated as

$$\Delta H' \approx [4(\Delta P')^2]^{1/2} = 0.016 \text{ mm} \quad (5)$$

With the foregoing estimates of the parameters in (1) and their probable errors, the terms of the right-hand side of (2) can be evaluated to check their relative importance. Table 2 lists their calculated values. It is clear that the first term is by far the most important for wide angle photography; errors due to $\Delta H'$, primarily owing to photoresolution, should dominate over the three sources of error in overall model scale. Elevation differences in this model would have to be stated with ±1300 meters independent of their magnitude.

For the narrow angle photography, ΔVAR should result in an uncertainty in elevation differences of about 4.5% (225 meters in 5000 meters) in addition to ±130 meters due to $\Delta H'$.

A shortened form of (2), including only the term due to $\Delta H'$, can be used to predict the scatter of relief determinations ΔH in our stereo models:

$$\Delta H \approx \frac{SR}{f \cdot \sin(VAR)} 1.6 \times 10^{-5} \text{ meters} \quad (6)$$

A slight elaboration of the meaning of (6) must be added. The ΔH calculated by (6) applies to a

TABLE 2. Calculated Values from Evaluation of Terms of Right-Hand Side of (2)

Coefficient	Probable Error	Contribution to Probable Error in H = 5000 meters, meters
	Wide Angle Camera	
$C_0 = 8 \times 10^7$	$\Delta H' = 0.016$ mm	$C_0\Delta H' = 1280$
$C_1 = 10^5$	$\Delta f(1\sigma) = 0.006$ mm	$C_1\Delta f = 0.6$
$C_2 = 2.5 \times 10^{-3}$	$\Delta SR = 10$ km	$C_2\Delta SR = 25$
$C_3 = 8.6 \times 10^3$ meters	$\Delta VAR = 0.15°$	$C_3\Delta VAR = 225$
	Narrow Angle Camera	
$C_0 = 8 \times 10^6$	$\Delta H' = 0.016$ mm	$C_0\Delta H' = 128$
$C_1 = 10^4$	$\Delta f(1\sigma) = 0.036$ mm	$C_1\Delta f = 0.36$
$C_2 = 2.5 \times 10^{-3}$	$\Delta SR = 10$ km	$C_2\Delta SR = 25$
$C_3 = 8.6 \times 10^3$ meters	$\Delta VAR = 0.15°$	$C_3\Delta VAR = 225$

stereo picture pair consisting of one picture taken from a vertical perspective and a second from an oblique perspective. If, instead, we have the more general case of two oblique pictures with the camera stations lying in a vertical plane at the target on opposite sides of the target, the cumulative relief displacement in the two pictures (subscripts 1 and 2) is

$$H_T' \equiv H_1' + H_2' \tag{7}$$

where, from (1),

$$\begin{aligned} H_1' &= H \cdot \sin(VAR_1) \cdot (f_1/SR_1) \\ H_2' &= H \cdot \sin(VAR_2) \cdot (f_2/SR_2) \end{aligned} \tag{8}$$

Thus H and ΔH are given by more general forms of (1) and (6):

$$H = \frac{H_T'}{\left[\frac{f_1}{SR_1} \cdot \sin(VAR_1) + \frac{f_2}{SR_2} \cdot \sin(VAR_2)\right]} \tag{9}$$

$$\Delta H = \frac{1.6 \times 10^{-5} \text{ meters}}{\left[\frac{f_1}{SR_1} \cdot \sin(VAR_1) + \frac{f_2}{SR_2} \cdot \sin(VAR_2)\right]} \tag{10}$$

In the most general case the camera stations of a stereo pair do not lie in a plane intersecting the ground target vertically. Then only the components of VAR_1 and VAR_2 in a vertical plane at the target contribute to relief determinations. In Figure 2 we represent the ground target, the camera stations, and the ground trace of a vertical plane through the target, labeled "Great Circle. We now find the components of VAR_1 and VAR_2 in this plane. This is most easily done by using a well-known identity for right spherical triangles. In Figure 2 the two perpendicular components of VAR_1 are designated ϕ_1 (in our vertical plane) and ω_1 (opposite angle W_1). Then ϕ_1 is given by

$$\tan(\phi_1) = \tan(VAR_1) \cos(W_1) \tag{11a}$$

similarly

$$\tan(\phi_2) = \tan(VAR_2) \cos(W_2) \tag{11b}$$

By using (1), (6), (11a), and (11b), we obtain generalized forms of (1) and (6):

$$H = \frac{H_T'}{\left[\frac{f_1}{SR_1} \cdot \sin(\phi) + \frac{f_2}{SR_2} \cdot \sin(\phi_2)\right]} \tag{12}$$

$$\Delta H = \frac{1.6 \times 10^{-5} \text{ meters}}{\left[\frac{f_1}{SR_1} \cdot \sin(\phi_1) + \frac{f_2}{SR_2} \cdot \sin(\phi_2)\right]} \tag{13}$$

Table 3 lists predicted errors in H for stereo models presented in the next part of this paper. These were calculated by using (13).

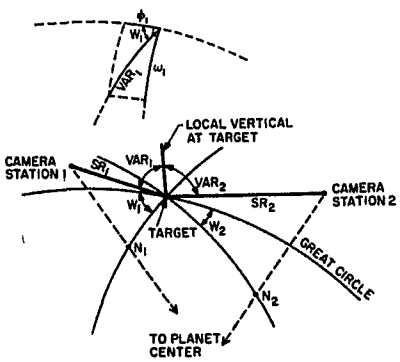

Fig. 2. Geometry of two camera stations from which a stereo pair of oblique pictures may be taken. The breakdown of the viewing angle VAR_1 into perpendicular components is illustrated. Only ϕ_1 contributes to relief determinations.

STEREO MODELS

The topography of a number of interesting Martian landforms has been derived by using our analytic technique of photogrammetry (see the appendix). This report has two purposes, the validation of the technique and a demonstration of the quality of the data for a more thorough analysis. We confine ourselves here to a minimum of geologic interpretation. Such interpretation and speculation is the continuing work of this author and many others both inside and outside the Mariner Mars 1971 Project.

The essentials of our first two stereo models, designated model 1 and model 2, are displayed pictorially in Figure 3, a photomosaic of a large volcanic cone with a central crater. This feature has been named Middle Spot, a reference to its two similar neighbors to the northeast and southwest and its dark dotlike appearance on low-resolution pictures of Mars taken early in the Mariner 9 mission. Centers of circles in Figure 3 mark point features whose elevations have been

TABLE 3. S

Model	Photomap Figure	Feature
1	3	Middle Spot
2	3	Middle Spot
3	6	Residual south pol
4	6	Residual south pol
5	7	Nix Olympica
6	8	Intratrough ridge

determined analytically. Using
have been able to establish
stereo models of Middle Spo
kilometers are given in parenth
circles as (1, 2) derived from mo
respectively. One point has b

Fig. 3. A mosaic of the
rectified to a vertical persp
analytic photogrammetry fr
4184-60, DAS 07111198.)

TABLE 3. Stered Models of Martian Topography Presented in This Paper

Model	Photomap Figure	Feature	Approximate Location	Photo DAS Time	Camera Focal Length, mm	Observed General Error in Model Elevations, meters	ΔH Predicted Error Calculated from (13), meters
				3858340	500.64		
1	3	Middle Spot	113.°W, 0.5°N	8585894	52.267	200	300
				4402135	52.267		
2	3	Middle Spot	113.°W, 0.5°N	7111128	52.267	400	700
				6029803	500.64		
3	6	Residual south polar cap	356.°W, 86.3°S	8331829	500.64	300	120
				5741963	500.64		
4	6	Residual south polar cap	5.°W, 86.8°S	7791983	500.64	300	130
				5492378	52.267		
5	7	Nix Olympica	133.°W, 18.°N	6823918	52.267	1000	1350
				10132929	500.64		
6	8	Intratrough ridge	87.1°W, 7.3°S	7326763	500.64	90	130

determined analytically. Using four pictures, we have been able to establish two independent stereo models of Middle Spot. Elevations in kilometers are given in parentheses next to the circles as (1, 2) derived from model 1 and model 2, respectively. One point has been chosen arbitrarily as the zero elevation for both models. The photo identification numbers and other information concerning the models are given in Table 3. The column labeled general error in model elevations contains a figure that is half the largest spread of values for the relief between

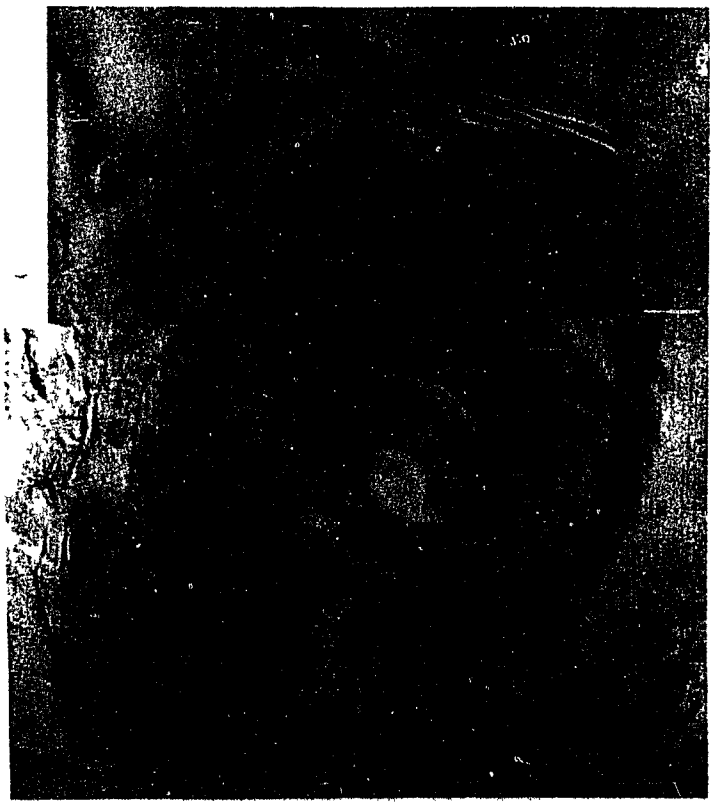

Fig. 3. A mosaic of the Martian volcanic shield Middle Spot. The pictures have been rectified to a vertical perspective. Point elevations in parentheses have been determined by analytic photogrammetry from models 1 and 2 (1, 2). (MTVS 4184-54, DAS 07111128; MTVS 4184-60, DAS 07111198.)

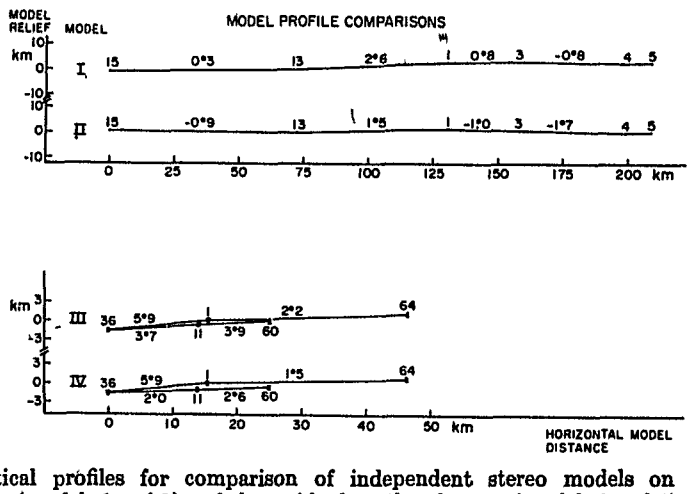

Fig. 4. Vertical profiles for comparison of independent stereo models on Middle Spot (models 1 and 2) and the residual south polar cap (models 3 and 4).

two points. The sample in a model was always too small to calculate a meaningful formal error such as a standard deviation, and so this estimate was adopted. Note that, for most models, this figure is within a factor of 2 of the predicted error ΔH.

A validation of the analytic technique is the essential agreement of independent stereo models except for a general tilt of one model in relation to the other. This is demonstrated to be the case for models 1 and 2 by the profiles in Figure 4. The 15-13 section of each profile is approximately perpendicular to the remainder, and so we are able to estimate the two components of the relative tilt of the models. From the general error for model elevations given in Table 3 we have calculated the slope differences and uncertainties along the profile. These are listed in Table 4. We observe that model 2 disagrees with model 1 only by a relative tilt of about 1.2° to the west around the 13-5 axis and 1.2° to the north about the 13-15 axis.

Let us now turn our attention to other profiles of Middle Spot in Figure 5. The low

TABLE 4. Systematic Differences in Topography between Models 1 and 2

Profile Section	Slope		Slope Difference = Relative Tilt of Models
	Model 1	Model 2	
13-15	0.3° ± 0.2°	-0.9° ± 0.3°	1.2° ± 0.4°
13-1	2.6° ± 0.2°	1.5° ± 0.3°	1.1° ± 0.4°
1-3	0.8° ± 0.4°	-1.0° ± 0.8°	1.8° ± 0.9°
3-4	-0.8° ± 0.3°	-1.7° ± 0.5°	0.9° ± 0.6°

slopes on the flanks of the cone and the total relief of about 10 km point to the basaltic shield volcano as the closest earthly analog. A group of basaltic shields, the island of Hawaii, stands approximately 10 km above the sea floor, and unmodified slopes range from 2° to 12° [*Macdonald*, 1972]. The central crater of Middle Spot, approximately 47 km across, is, however, much larger than those associated with earthly shield volcanoes. For example, the summit caldera of Mauna Loa measures only 2.4 × 4.8 km.

A second pair of overlapping stereo models, on the residual south polar cap, is presented in Figure 6. Figure 4 contains profiles common to these two models. Again we can account for the differences in the profiles with a simple tilt of one model in relation to the other. The axis of the tilt appears to run through points 36 and 1.

The residual south polar cap is an area of surface frost observed to persist through the southern hemisphere summer in 1971–1972. The dark strips of defrosted terrain running through the cap suggest that the underlying materials are the same as those of a very widespread polar geologic unit now designated laminated terrain [*Murray et al.*, 1972]. The name is derived from the narrow parallel bands that seem to follow the contours of the topography. On pictures of the region of Figure 6, which have been specially processed to bring out de-

tail in the dark areas, it is poss
bands in the wide defrosted st
and three bands on the narr
southwest. If these bands rep
geologic units, it becomes imp
mate the total relief across a d
place some constraints on the de
ess. We will attempt this for
frosted strip using the profiles
Figure 5.

Because surfaces of equal el
topographic model differ from
on Mars only by a small tilt, v
the relief across the dark strips
tematically untilt straight prof
least three points. For example,
is shown in Figure 5. Points 65
one side of the strip, and point
other. We assume that points
in the same horizontal surface
ject that surface on to point 92
culated to lie 175 meters below
level. This assumption of very
the continuously frosted area
systemic changes in slope obser
crossing both defrosted strips. R
narrow strip has been calculatec
files (Table 5). The stereo mo
slope downward toward the sout
lief of the order of 200 meters.

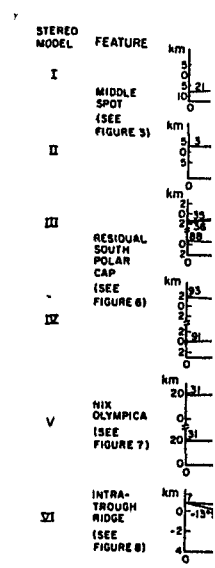

Fig. 5. Vertical prof

tail in the dark areas, it is possible to see eight bands in the wide defrosted strip to the east and three bands on the narrow strip in the southwest. If these bands represent stratified geologic units, it becomes important to estimate the total relief across a defrosted strip to place some constraints on the depositional process. We will attempt this for the narrow defrosted strip using the profiles for model 4 in Figure 5.

Because surfaces of equal elevation in our topographic model differ from such surfaces on Mars only by a small tilt, we can estimate the relief across the dark strips only if we systematically untilt straight profiles through at least three points. For example, profile 65-69-92 is shown in Figure 5. Points 65 and 69 lie on one side of the strip, and point 92 lies on the other. We assume that points 65 and 69 lie in the same horizontal surface and then project that surface on to point 92, which is calculated to lie 175 meters below that reference level. This assumption of very low relief in the continuously frosted area is justified by systemic changes in slope observed on profiles crossing both defrosted strips. Relief across the narrow strip has been calculated for four profiles (Table 5). The stereo model indicates a slope downward toward the southwest with relief of the order of 200 meters.

Before passing on to another Martian feature, we note the anomalous relationship of the general model error to the calculated ΔH for the south polar cap models. The observed error is approximately twice the predicted error. This discrepancy may be attributed to the nature of the features used in these models. Instead of fixed point features such as crater centers, which were commonly used elsewhere on Mars, we have used dark spots of defrosted ground and albedo markings within the frost. Such features have the unfortunate property of changing size and shape significantly with time, tending to increase $\Delta H'$.

Model 5 shown in Figure 7 is another Martian volcano, Nix Olympica. The slopes shown in the profiles of Figure 5 are similar in angle to those of Middle Spot, but the base of the cone is larger, and so the total relief from the top of the basal scarp (point 9) to the rim of the complex caldera is about 20 km, twice that of any similar feature on the earth.

Model 6 shown in Figure 8 represents the limits of precision attainable from Mariner 9 data. A pair of high-resolution pictures taken near periapsis were used in its construction. The area is part of the Coprates canyon or trough system that stretches 4800 km across Mars between the equator and 20°S. The plateau shown sits inside a trough over 200 km

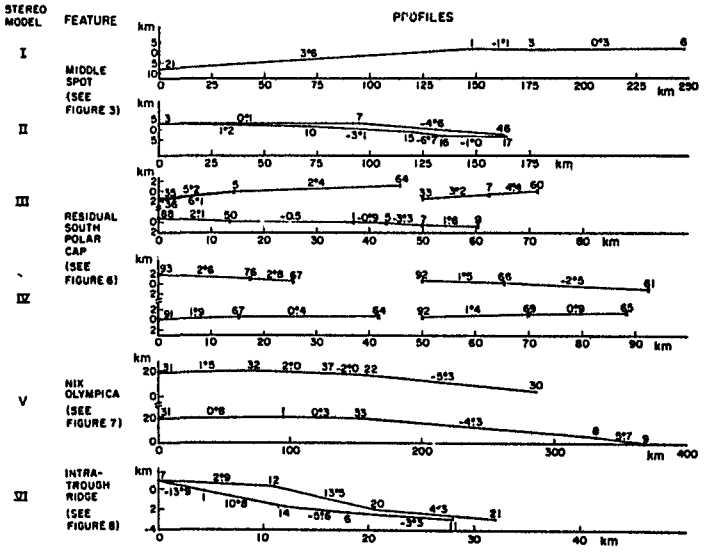

Fig. 5. Vertical profiles of Martian surface features from six stereo models.

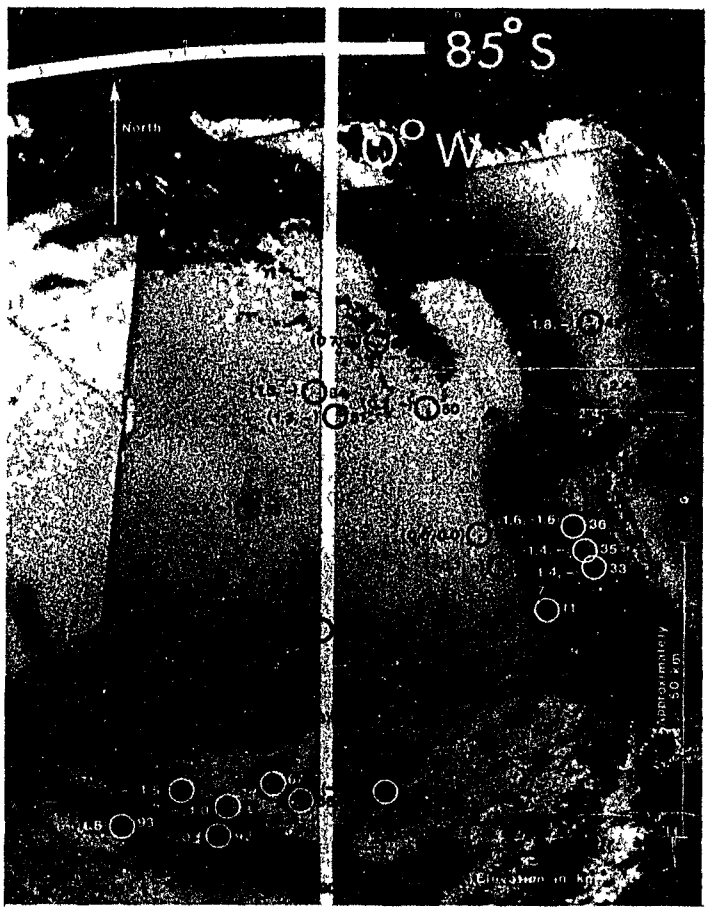

Fig. 6. A mosaic of pictures of the residual south polar cap rectified to a polar stereographic projection. Point elevations in parentheses have been determined by analytic photogrammetry from models 3 and 4 (3, 4). (MTVS 4149-21, DAS 06029803; MTVS 4221-06, DAS 08331829; MTVS 4140-27, DAS 05741963; MTVS 4205-102, DAS 07791983.)

wide. The craters on its upper surface resemble those outside the canyon and suggest that this was once part of a continuous stretch of cratered terrain that has been partially destroyed by the canyon-forming process. The local relief, about 3.5 km, represents material removed to create the trough. The slopes, up to at least 13.9°, are distinctly steeper than those seen on the flanks of the volcanoes but are not particularly steep by earth standards.

Although it has demonstrated a useful technique and tested the quality of topographic data from Mariner 9 pictures, this paper has made only a small contribution to data reduction. We must now start the task of sorting out the stereo coverage on interesting features and determining which photogrammetric techniques to apply. Such work will certainly take years, and the larger task of geologic interpretation will proceed for decades.

TABLE 5. Estimating Relief across a Defrosted Strip within the Residual South Polar Cap

Profile	Points Held Level	Derived Relief across Defrosted Strip, meters
61-66-92	61,66	270
67-76-93	67,76	54
65-69-92	65,69	175
64-67-91	64,67	400

APPENDIX

A scheme for describing oblique pictures. Figure 9 quantities that are important f tion of relief between point an oblique picture. For this rep present the relations derived f and defer an outline of their other place. The relief shown the vertical distance H, which i quantities in the diagram by t

$$H = (H' \cdot SR)/x \cos (SUBR$$

where the quantities are define

H vertical relief to be d
H' relief displacement from its foot, i.e., t image of H in the foc
SR slant range, from th feature H.

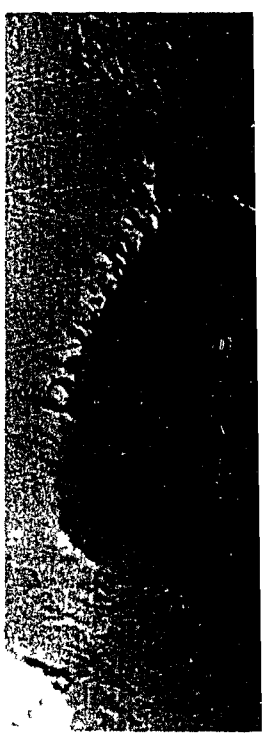

Fig. 7. A slightly oblique tions in parentheses have b DAS 06823918.)

APPENDIX

A scheme for describing the geometry of oblique pictures. Figure 9 contains all the quantities that are important for the determination of relief between point features seen in an oblique picture. For this report I shall merely present the relations derived from this diagram and defer an outline of their derivation to another place. The relief shown in Figure 9 is the vertical distance H, which is related to other quantities in the diagram by the basic relation

$$H = (H' \cdot SR)/x \cos(SUBR)/\sin(VAR) \tag{A1}$$

where the quantities are defined:

- H vertical relief to be determined.
- H' relief displacement of the crest of H from its foot, i.e., the length of the image of H in the focal plane.
- SR slant range, from the camera to the feature H.
- x distance from the optic center of the lens to the image of H in the focal plane.
- $SUBR$ angle between a line, perpendicular to the direction of H' and passing through the optic center of the lens, and the optic path to feature H.
- VAR emission angle at the surface at feature H.

The quantities SR, x, $SUBR$, and VAR from which H is calculated are all derived from a more fundamental set of quantities describing the position and orientation of the camera when photographing H. There is a great deal of flexibility in the choice of this set, but, as an example, we shall use the following:

- R radius of the planet at feature H.
- $RMAG$ range from the spacecraft to the center of the planet.
- TA tilt angle, the angle between the camera axis and the direction to the center of the planet.

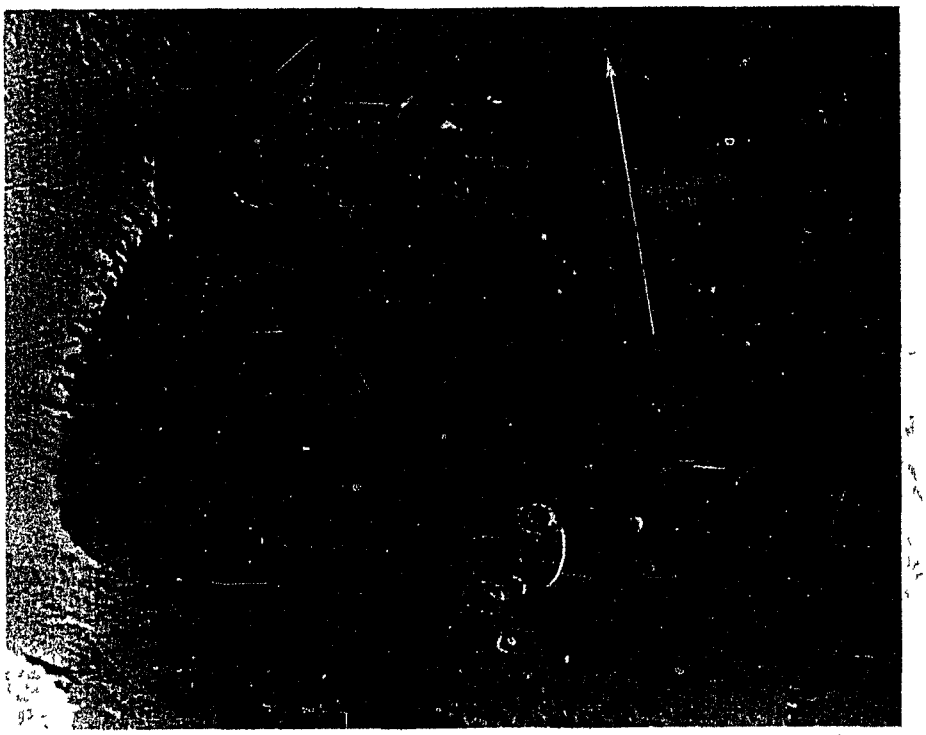

Fig. 7. A slightly oblique view of part of the volcanic shield Nix Olympica. Point elevations in parentheses have been determined by analytic photogrammetry. (MTVS 4174-93, DAS 06823918.)

Fig. 8. A nearly vertical view of a flat topped ridge rising from the bottom of the Coprates trough or canyon. Point elevations in parentheses have been determined by analytic photogrammetry. (MTVS 4191-42, DAS 07326763.)

f focal length of the camera.
L, K coordinates of the image of feature H in the focal plane.

The quantities in (A1) are related to the above by:

$$x = (K^2 + L^2 + f^2)^{1/2} \quad \text{(A2)}$$

$$SUBR = \tan^{-1}[(SI - SIA)/x] \quad \text{(A3}a\text{)}$$

$$SI \equiv \left\{K^2 + [f \cdot \tan(TA) + L]^2\right\}^{1/2} \quad \text{(A3}b\text{)}$$

$$SIA \equiv f \cdot \tan(TA)[1 - (K/SI)^2]^{1/2} \quad \text{(A3}c\text{)}$$

$$VAR = \sin^{-1}[(RMAG/R) \cdot \sin(NAA)] \quad \text{(A4}a\text{)}$$

$$NAA \equiv SUBR + SUA \quad \text{(A4}b\text{)}$$

$$SUA \equiv \tan^{-1}(SIA/x) \quad \text{(A4}c\text{)}$$

$$SR = R \cdot \sin(VAR - NAA)/\sin(NAA) \quad \text{(A5)}$$

The relationships among the quantities of (A3), (A4), and (A5) are exhibited in Figures 10 and 11.

The determination of relief of surface features. Because real geologic features do not consist of upright posts or vertical scarps that would be imaged as H is in Figure 9, we must somehow infer a relief displacement H' for a feature, for example, a hilltop, that is the image of the relief of the hilltop above some point at its base. This is possible if we have a second picture of the same feature taken from a different perspective. Figure 12 consists of schematic diagrams of two such pictures of a hypothetical feature. Points A and B represent point features at the crest and foot of a hill, respectively, imaged in two separate pictures. We wish to derive the vertical relief along traverse AB. This is imaged as H_1' in (a) and H_2' in (b), but the point C defining the length of H_1' and H_2' is not imaged in the pictures as it is below the ground surface vertically beneath point A at the elevation of point B. The location of point C in a picture is inferred from two facts. (1) It is located on a line joining A and the nadir

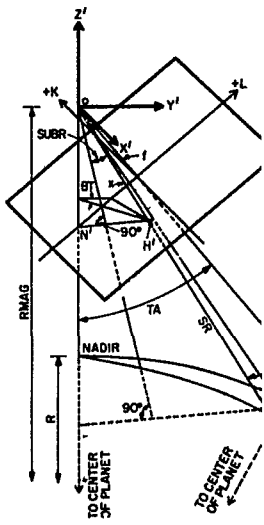

Fig. 9. The geometry of r
a planetary scale oblique pic
on *Imhof and Doolittle* [1966]

point N'. An axiom of photo
is obvious from Figure 9,
placement is radially outwa
point. (2) The ground dist
from the image lengths BC_1
pictures must be the same.
is to find a pair of distances
H_1', and H_2', which represe

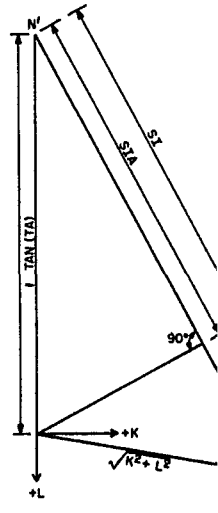

Fig. 10. The geometry of
the focal plane of an oblique
tions are given by (A3) and (A

bottom of the
determined by

xhibited in Figures

ief of surface fea-
c features do not
rertical scarps that
Figure 9, we must
lacement H' for a
p, that is the image
bove some point at
we have a second
aken from a differ-
nsists of schematic
s of a hypothetical
present point fea-
a hill, respectively,
tures. We wish to
long traverse AB.
and H_2' in (*b*), but
gth of H_1' and H_2'
as it is below the
neath point A at
e location of point
om two facts. (1)
g A and the nadir

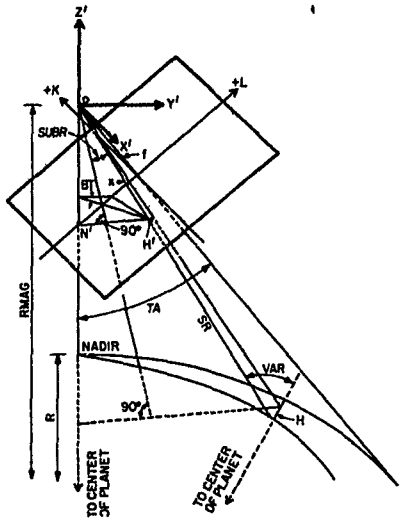

Fig. 9. The geometry of relief H imaged in a planetary scale oblique picture (partly based on *Imhof and Doolittle* [1966]).

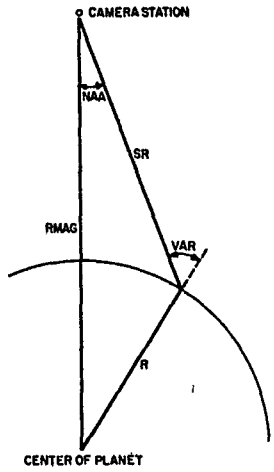

Fig. 11. The geometry of some quantities in the principal plane (the plane containing the camera axis and the nadir) of an oblique picture (A5).

point N'. An axiom of photogrammetry, which is obvious from Figure 9, is that relief displacement is radially outward from the nadir point. (2) The ground distance $\overline{BC}$ derived from the image lengths $\overline{BC_1}'$ and $\overline{BC_2}'$ in the pictures must be the same. The problem now is to find a pair of distances in the focal plane, H_1', and H_2', which represent the same value of H according to (A1) and give identical horizontal ground distances from the consequent image lengths $\overline{BC_1}'$ and $\overline{BC_2}'$. Because of the nonlinear nature of (A1)–(A5), I have adopted an iteration procedure. Briefly it is: (1) pick an H_1' and calculate H from (A1), (2) calculate H_2' from (A1), (3) calculate the ground distance $\overline{BC}$ for each photo from $\overline{BC_1}'$ and $\overline{BC_2}'$,

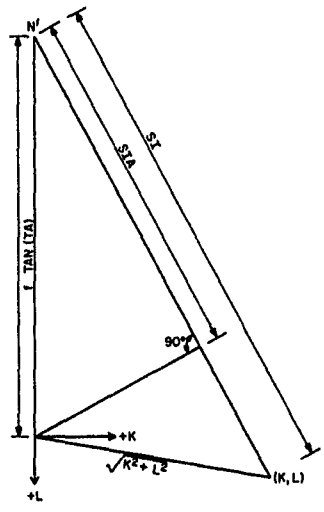

Fig. 10. The geometry of some quantities in the focal plane of an oblique picture. Some relations are given by (A3) and (A4).

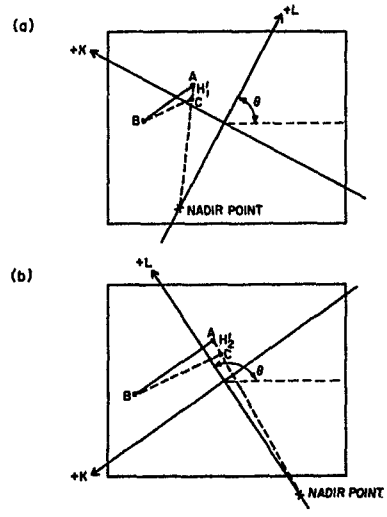

Fig. 12. Schematic diagrams of a topographic feature observed in two oblique pictures.

and (4) use the value of $(\overline{BC}_1 - \overline{BC}_2)$ to correct H_1'.

All that remains to implement the above procedure is to outline a technique for the derivation of the horizontal ground distance $\overline{BC}$ from its image (step 3) as above. One scheme is to find the difference of vectors from the spacecraft to B and C. The coordinate system of these vectors, centered at 0, is shown in Figure 9. If we label the vectors to B and C as **B** and **C**, respectively, their components can be derived from Figure 9 as:

$$\begin{aligned} B_X &= SR_B \cdot \sin(NAA_B) \cdot \sin(BT_B) \\ NA_B &\equiv L + f \cdot \tan(TA) \\ BT_B &= \tan^{-1}[-K_B/(NA_B \cdot \cos(TA))] \\ B_Y &= SR_B \cdot \sin(NAA_B) \cdot \cos(BT_B) \\ B_Z &= SR_B \cdot \cos(NAA_B) \end{aligned} \quad \text{(A6)}$$

The components of **C** are similarly derived with the appropriate C subscript on parameters. The cord distance from B to C is just $|\mathbf{B} - \mathbf{C}|$. This deviates from the exact distance $\overline{BC}$, following the curvature of the planet, by less than 1 part in 10^3 for $\overline{BC} \lesssim 350$ km on Mars. This is adequate for out work on generally small features.

Consistency arguments to improve input parameters. If the values of the basic input parameters describing the geometry of a picture, *RMAG*, *TA*, and the orientation angle θ of the *K-L* coordinate system in Figure 12, are sufficiently imprecise, the elevations derived from point features may be contradictory. Let us designate as $H(a, b)$ the derived elevation of point a above point b. The contradictions we find are of the form of

$$H(1, 2) - H(1, 3) \neq H(4, 2) - H(4, 3) \quad \text{(A7)}$$

Given a sufficient number of point features in the stereo overlap region of a pair of pictures, we can devise any number of conditions, such as

$$H(1, 2) - H(1, 3) = H(4, 2) - H(4, 3) \quad \text{(A8)}$$

to control an iteration scheme to improve the values of any or all of *RMAG*, *TA*, and θ. The procedure is to hold these quantities constant for one of the pictures and let them vary for the other until conditions such as (A8) are satisfied to the desired accuracy. This procedure is commonly termed a relative orientation. It was required to establish models 3, 4, and 5 presented in the main body of this paper. Changes required in θ and *TA* were less than 0.5° in all cases, and only one model required adjustment in the nominal value of *RMAG*. Because the parameters of one picture were held constant, the resulting three-dimensional model of topography may have an overall tilt in relation to the local horizontal reflecting errors in *TA* and θ for that picture.

Caution must be exercised in the performance of a relative orientation with extremely narrow angle photography, such as that from the Mariner 9 narrow angle camera. D. W. G. Arthur (personal communication, 1973) pointed out that, in the extreme case, imaginary orthographic pictures, the angle between the camera stations measured from the ground target is indeterminate. The magnitude of this angle controls the scale of the stereo model, and so it should be held constant while performing a relative orientation. This constraint has been maintained in the construction of models in this paper that were derived from narrow angle photography.

Arthur has shown that the above restriction can be avoided if a minimum of three pictures of a feature can be employed. This author has not pursued this possibility, owing to the extreme rarity of such triple coverage by the Mariner 9 narrow angle camera.

Acknowledgments. I am indebted to all the people who combined their efforts to make Mariner Mars 1971 a successful mission. With respect to the work reported in this article, specific acknowledgment for aid must go to L. A. Soderblom and S. S. C. Wu of the U.S. Geological Survey, M. Benesh of the Jet Propulsion Laboratory, and B. Murray of the California Institute of Technology. The processed pictures used for this work were obtained and studied in a timely fashion only with the cooperation of J. Seidman, A. Schwartz, and J. Soha of JPL and J. J. van der Woude of Caltech.

REFERENCES

Imhof, R. K., and R. C. Doolittle, Mapping from oblique photographs, in *Manual of Photogrammetry*, p. 913, American Society of Photogrammetry, Falls Church, Va., 1966.

Macdonald, G. A., *Volcanoes*, Prentice-Hall, New Jersey, 510 pp., 1972.

Masursky, H., R. Batson, W. Borgeson, M. Carr, J. McCauley, D. Milton, R. Wildey, D. Wilhelms, B. Murray, N. Horowitz, R. Leighton, R. Sharp, W. Thompson, G. Br deysson, E. Shipley, C. Sagan, Lederberg, E. Levinthal, W. McCord, B. Smith, M. Davie couleurs, and C. Leovy, Televisi for Mariner Mars 1971, *Icarus, 1*

Murray, B. C., L. A. Soderblom, R. P. Sharp, D. J. Milton, and R Geological framework of the sout of Mars, *Icarus, 17*, 328, 1972.

R. Sharp, W. Thompson, G. Briggs, P. Chandeysson, E. Shipley, C. Sagan, J. Pollack, J. Lederberg, E. Levinthal, W. Hartmann, T. McCord, B. Smith, M. Davies, G. deVaucouleurs, and C. Leovy, Television experiment for Mariner Mars 1971, *Icarus, 12,* 10, 1970.

Murray, B. C., L. A. Soderblom, J. A. Cutts, R. P. Sharp, D. J. Milton, and R. B. Leighton, Geological framework of the south polar region of Mars, *Icarus, 17,* 328, 1972.

Snyder, L. M., Mariner 9 TV subsystem calibration report, *Doc. 610-202,* Jet Propul. Lab., Pasadena, Calif., 1971.

Wu, S. S. C., F. J. Schafer, G. M. Nakata, R. Jordan, and K. R. Blasius, Photogrammetric evaluation of Mariner 9 photography, *J. Geophys. Res., 78,* this issue, 1973.

(Received January 4, 1973;
revised March 14, 1973.)